J. Fluid Mech. (1996), vol. 320, pp. 19–51

Shear-free turbulence near a flat free surface

By D. T. WALKER,[1] R. I. LEIGHTON[2] AND L. O. GARZA-RIOS[1]

[1] Department of Naval Architecture and Marine Engineering, University of Michigan, Ann Arbor, MI 48109-2145, USA

[2] Remote Sensing Division, Naval Research Laboratory, Washington, DC, 20375-5351, USA

(Received 20 September 1994 and in revised form 30 January 1996)

In this study the evolution of initially homogeneous and isotropic turbulence in the presence of a free surface was investigated. The Navier–Stokes equations were solved via direct pseudo-spectral simulation with a resolution of 96^3. The Reynolds number based on the volume-averaged turbulence kinetic energy and dissipation rate was 147. Periodic boundary conditions were used in two dimensions, and the top and bottom sides of the domain were flat and shear-free. A random, divergence-free velocity field with a prescribed spectrum was used as the initial condition. An ensemble of sixteen separate simulations was used to calculate statistics.

Near the surface, the Reynolds stresses are anisotropic and the anisotropy extends a distance from the surface roughly equal to the turbulent lengthscale. The tangential vorticity fluctuations also vanish near the surface, owing to the no-shear condition, causing a corresponding decrease in the fluctuating enstrophy. The thickness of the region in which the surface affects the vorticity distribution is roughly one-tenth the turbulent lengthscale. The stress anisotropy near the surface appears to be maintained by reduced dissipation for the tangential velocity fluctuations, reduced pressure–strain transfer from the tangential to surface-normal velocity fluctuations, and rapid decay of the surface-normal velocity fluctuations due to dissipation. The turbulence kinetic energy rises in the near-surface region owing to a decrease in dissipation at the surface. This decrease in dissipation results from the local reduction in enstrophy owing to the vanishing of the tangential vorticity fluctuations at the surface. At the free surface, the mean pressure rises. This is also due to the reduction in enstrophy.

While the tangential vorticity must vanish at the free surface, the flow is fully three-dimensional up to the surface and the production of surface-normal vorticity by vortex stretching attains a maximum at the free surface. The contribution to the total enstrophy by the surface-normal vorticity fluctuations remains relatively constant over depth. The production of the surface-normal enstrophy component due to vortex stretching is roughly balanced by turbulent transport of enstrophy away from the surface. Near the surface, there are elevated levels of production of tangential vorticity by both vortex-stretching and fluctuating shear strains.

1. Introduction

Many situations of engineering interest result in turbulent flow of a liquid near a liquid–gas interface, a free surface. These flows include the near-surface layer of the ocean, a stirred fluid within a vessel, and many which occur in materials-processing procedures. At a free surface, the relative velocity between the fluid and the interface must vanish. In addition, the tangential stress at the surface must vanish, and the normal stress must balance the ambient pressure above the surface. As a result, when

a turbulent flow interacts with a free surface, the velocity field is significantly altered. For turbulent shear flows, the free surface alters the mean velocity as well as the turbulence. This can obscure the effects of the free surface on the turbulence. In this study we examine the evolution of shear-free, initially homogeneous turbulence near a free surface. In this way, the interaction of the turbulence with a free surface can be examined without the complicating effects of the mean-flow/free-surface interaction.

In this study, the Navier–Stokes equations were solved via direct pseudo-spectral simulation with a resolution of 96^3. The computational domain was a cube $4.25L$ on a side, where $L = \tilde{k}/\tilde{\epsilon}^{3/2}$ is the turbulent lengthscale (here $\tilde{k}$ and $\tilde{\epsilon}$ are the volume-averaged turbulence kinetic energy and dissipation rate). Periodic boundary conditions were used in two dimensions, and the top and bottom sides of the cube were flat and shear-free. A random, divergence-free velocity field with a prescribed spectrum was used as the initial conditions. The free-surface boundary conditions were applied to this initially homogeneous isotropic velocity field. An ensemble of 16 simulations was used to calculate turbulence statistics. The flow was examined at late times, after the effect of the boundary 'insertion' had diminished. At this time the turbulent Reynolds number (based on $\tilde{\epsilon}$ and $\tilde{k}$) was 147; the microscale Reynolds number was about thirty. The free surface is flat, which corresponds to the limit of either zero Froude number or zero Weber number (infinite gravity or surface tension, respectively).

Various turbulent shear flows near free surfaces have been examined in recent years. Turbulent open channel flow, in which turbulence generated at a solid bottom wall interacts with the free surface, was examined by Lam & Banerjee (1988) and Handler *et al.* (1993), among others. Turbulent jets interacting with a free surface have been investigated by Swean *et al.* (1989), Anthony & Willmarth (1992), Madnia & Bernal (1994), Mangiavacchi, Gundlapalli & Akhavan (1994), Leipmann & Gharib (1994) and Walker, Chen & Willmarth (1995). Uzkan & Reynolds (1967) and Thomas & Hancock (1977) examined homogeneous grid-generated turbulence interacting with a moving solid wall. (This flow has a homogeneous mean flow, but has a no-slip boundary condition at the wall rather than a vanishing-shear condition.)

Shear-free turbulence near a free surface has been studied experimentally, numerically and theoretically. The early evolution of turbulence near a solid wall with zero mean shear has been considered theoretically by Hunt & Graham (1978). The relevant part of their analysis treats the boundary as shear free, and therefore is applicable to free-surface flows. They found that the tangential velocity fluctuations are elevated over a region roughly half the integral scale of turbulence, and the surface-normal fluctuations are reduced over a region which is about twice as thick. Their results indicated that there is a loss of energy from the low-wavenumber portion of the one-dimensional spectrum of the surface-normal velocity fluctuations. The gain in energy in the spectrum of the tangential velocity fluctuations occurs at higher wavenumber. At the surface, the turbulence kinetic energy is equal to that far from the boundary, but there is a small decrease in energy near the surface owing to the larger region of decreased $\overline{w^2}$ relative to the thickness of the region where $\overline{u^2}$ is elevated. In contrast to those results, we will show that at late times the regions where the tangential and surface-normal velocity fluctuations are altered are of comparable thickness, and that the turbulence kinetic energy actually rises near the surface. The rise in kinetic energy results from a reduction in dissipation locally at the boundary, an effect which is not captured in the theory.

Brumley & Jirka (1987) investigated a stirred fluid with zero mean velocity, generated by an oscillating grid below a free surface. Their results confirmed the occurrence of anisotropy near the surface, and they compared to the theoretical results

of Hunt & Graham (1978). Their results were in approximate agreement with the theory for the stress anisotropy, although the comparison was complicated by the inhomogeneity of the oscillating grid flow in the direction normal of the free surface.

Perot & Moin (1993, 1995) used direct numerical simulation to examine initially homogeneous turbulence near a flat bounding surface which was either a solid wall, a free surface, or a permeable membrane. They examined early times after the insertion of the boundary into an initially homogeneous and isotropic flow (the time after boundary insertion is roughly one-third of that examined in the present study), and the turbulent Reynolds numbers ranged from 6.2 to 134 (which approaches the value for the present study). Their conclusions regarding free surface flows were that the increase in the tangential velocity fluctuations at the surface was a result of a local decrease in dissipation, and that the decrease in the surface-normal velocity fluctuations near the free surface is due to increased turbulent transport, including pressure transport. In addition, they concluded that the pressure–strain correlations, normally assumed to be the dominant mechanism for energy redistribution in the near-surface region, contributes little to the observed anisotropy.

Perot & Moin discussed the near-surface energy redistribution in terms of two structures: the 'splat' which is comprised of fluid moving toward the free surface (after Bradshaw & Koh 1981) and the 'anti-splat' which they describe as regions of fluid ejecting downward, away from the free surface. They asserted that the net level of redistribution is determined by the balance between splats and anti-splats, and that this balance is set by viscous effects. In the case of a free surface (*vs.* a solid wall or permeable membrane) they surmise that the splats and anti-splats are roughly in balance (owing to the lack of viscous effects which would result from a no-slip boundary), and so pressure–strain redistribution is relatively unimportant compared with other effects such as turbulent transport.

In the present study, we find that the degree of anisotropy near the surface appears to be maintained, in part, by reduced dissipation for the tangential velocity fluctuations (as concluded by Perot & Moin), but also by the reduction in pressure–strain transfer from the tangential to surface-normal velocity fluctuations caused by the free surface and rapid temporal decay of the surface-normal velocity fluctuations. This latter effect is due to the fact that the surface-normal velocity fluctuations vanish at the surface, while their dissipation rate remains finite. The results of the present study also show that for the surface-normal velocity fluctuations, the pressure transport and the turbulent transport due to velocity fluctuations roughly balance and result in little net turbulent transport. In the discussion of the Reynolds-stress balances, presented below in §3.2.3 we argue that the net level of pressure–strain redistribution (and presumably the balance between splats and anti-splats) is affected by the local level of stress anisotropy. This is in addition to the role of viscous effects discussed by Perot & Moin.

Gharib, Dabiri & Zhang (1994) examined temporally decaying turbulence generated by a moving grid. On the basis of experimental measurements of the vector velocity field in planes parallel to the free surface, they concluded there was a region of quasi-two-dimensional turbulence near the free surface which is characterized by a reverse energy cascade, and vortex amalgamation leading to an enstrophy increase at the free surface. At some distance below the free surface, the turbulence becomes fully three-dimensional. The results of the present study indicate that, while the tangential vorticity must vanish at the free surface, the flow is fully three-dimensional up to the surface and that the production of surface-normal vorticity by vortex stretching (which is inconsistent with the idea of two-dimensional turbulence) attains a maximum at the free surface. The contribution to the total enstrophy by the surface-normal vorticity

fluctuations remains relatively constant over depth, which is in contrast to the results of Gharib *et al.* (1994).

In addition to these results, we will show that the tangential vorticity vanishes in an extremely thin layer adjacent to the free surface. The vanishing tangential vorticity at the surface causes a reduction in the fluctuating enstrophy near the surface. This reduction in enstrophy is the root cause of the near-surface decrease in dissipation which leads to the increased turbulence kinetic energy mentioned above. The reduced enstrophy also causes an increase in the mean pressure near the surface. We also show that production of tangential vorticity fluctuations by vortex-stretching, and by the fluctuating shear strains, is significant near the surface, and can be related to different types of motions in the fluid.

2. Computational method and calculation of the statistical quantities

The results presented below were obtained via direct numerical solution of the three-dimensional time-dependent Navier–Stokes equations. Here, we discuss the computational method, how the simulation was initialized, the temporal decay of the turbulence, the initial conditions for the ensemble of simulations, and finally, how the statistics were calculated.

2.1. *Computational method*

The incompressible Navier–Stokes equations were solved using a pseudo-spectral method. In this scheme, which follows from Orszag & Patera (1983) and Kim, Moin & Moser (1987), the equations of motion are solved in rotational form by expanding the velocity field in a series of orthogonal functions. Elimination of pressure from the governing equations gives rise to a fourth-order partial differential equation for the surface-normal velocity and a second-order partial differential equation for the surface-normal vorticity. This formulation of the problem ensures that the continuity equation is satisfied at each timestep and, in this sense, it differs from other methods in which operator splitting is used. Chebyshev polynomials are used in the direction normal to the free surface and Fourier expansions are used in the two horizontal directions. A Chebyshev–tau approximation is used to solve the Poisson equations arising in the problem formulation. Crank–Nicholson time stepping is used for the viscous operator and the second-order Adams–Bashforth scheme is used for the nonlinear terms.

The free surface is treated as a flat, shear-free boundary. Such a boundary occurs in the absence of atmospheric forcing and in the limit of zero Froude number and Weber number. The formulation of the problem requires two boundary conditions for the normal velocity and one condition for the normal vorticity on the top and bottom boundaries. Both boundaries are flat so the surface-normal velocity must vanish, i.e. $w = 0$. From the requirement of no tangential stress, and the definition of vorticity and continuity, the remaining conditions are $\partial^2 w/\partial z^2 = 0$, where z is the surface-normal coordinate, and $\partial \omega_z/\partial z = 0$, where ω_z is the surface-normal vorticity. In the homogeneous directions, the flow is assumed periodic. In post-processing the data to obtain the pressure field, Neumann pressure boundary conditions at the free surface were obtained from the surface-normal component of the Navier–Stokes equations.

2.2. *Initial conditions*

To generate useful statistical quantities, an ensemble of sixteen independent flows was calculated and the results ensemble averaged. A homogeneous isotropic velocity field was first established. The free-surface boundaries were then inserted and the velocity

field was allowed to evolve for a short time. The sixteen independent flows were then generated from this one. These flows were allowed to evolve for an additional period of time and formed the basis for the results presented below.

The homogeneous isotropic velocity field was established by requiring that the initial velocity spectrum have a prescribed form and that the Fourier-transformed velocity field be random Gaussian variables. The approach is similar to that of Orszag (1969). The constraints of reality of the flow and continuity must also be satisfied by the initial conditions. The transformed velocity field is related to the spectrum by

$$\Phi_{ij}(k_m) = \overline{u_i(k_m)\, u_j(k_m)} = \frac{E(k)}{4\pi k^2}\left(\delta_{ij} - \frac{k_i k_j}{k^2}\right), \tag{1}$$

where k_i is the wave vector and $k = (k_i k_i)^{1/2} \cdot E(k)$ is the initial one-dimensional spectrum; for this case, the von Kármán spectrum was used (Hinze 1975, p. 244). To calculate the initial velocity field, Gaussian random fields Q_i were scaled by the square root of the spectrum function and projected into divergence-free space:

$$\hat{u}_j(k_m) = P_{ij}(k_m)\left(\frac{E(k)}{4\pi k^2}\right)^{1/2} Q_i(k_m), \tag{2}$$

where

$$P_{ij}(k_m) = \delta_{ij} - \frac{k_i k_j}{k^2} \tag{3}$$

is the projection operator in Fourier space. This initial velocity field, determined on a uniform grid in physical space, was then interpolated onto the Gauss–Labatto grid in direction normal to the free surface.

The choice of the initial spectrum defines lengthscales and velocity scales for the computation. For this simulation, the lengthscale was the initial integral scale (i.e. the integral of the longitudinal correlation function $R_{11}(x_1)$) and the velocity scale was the r.m.s. velocity (the square of the r.m.s. velocity is two-thirds the turbulence kinetic energy). A computational time unit is the ratio of these two quantities. This timescale is used to describe the results in this section. The detailed presentation of the results in §3 uses the large-eddy timescale as defined below.

In establishing this initial velocity field, no attempt was made to enforce the free-surface boundary conditions. As discussed by Perot & Moin (1993), the insertion of the free-surface boundaries so perturbs the flow that the timesteps must be extremely small in order to prevent numerical instability. This results in a fairly expensive calculation. To avoid this, a single simulation was allowed to evolve for five time units after boundary insertion. At this point in time, the effects of the boundary insertion (but not the effects of the free-surface boundary itself) have diminished, and the flow has evolved sufficiently long to be representative of homogeneous isotropic turbulence in the centre portion of the computational domain.

This velocity field (which had evolved for five computational time units) was used to construct the initial conditions for the ensemble of sixteen flows used in calculating the statistics presented below. To generate the statistically independent velocity fields, the surface-normal velocity and vorticity were Fourier-transformed in planes parallel to the free surface (x, y-planes) and the each of the Fourier coefficients was multiplied by a different random complex number of unit magnitude (and different numbers were used for velocity and vorticity). This alters the phase of the complex Fourier coefficient.

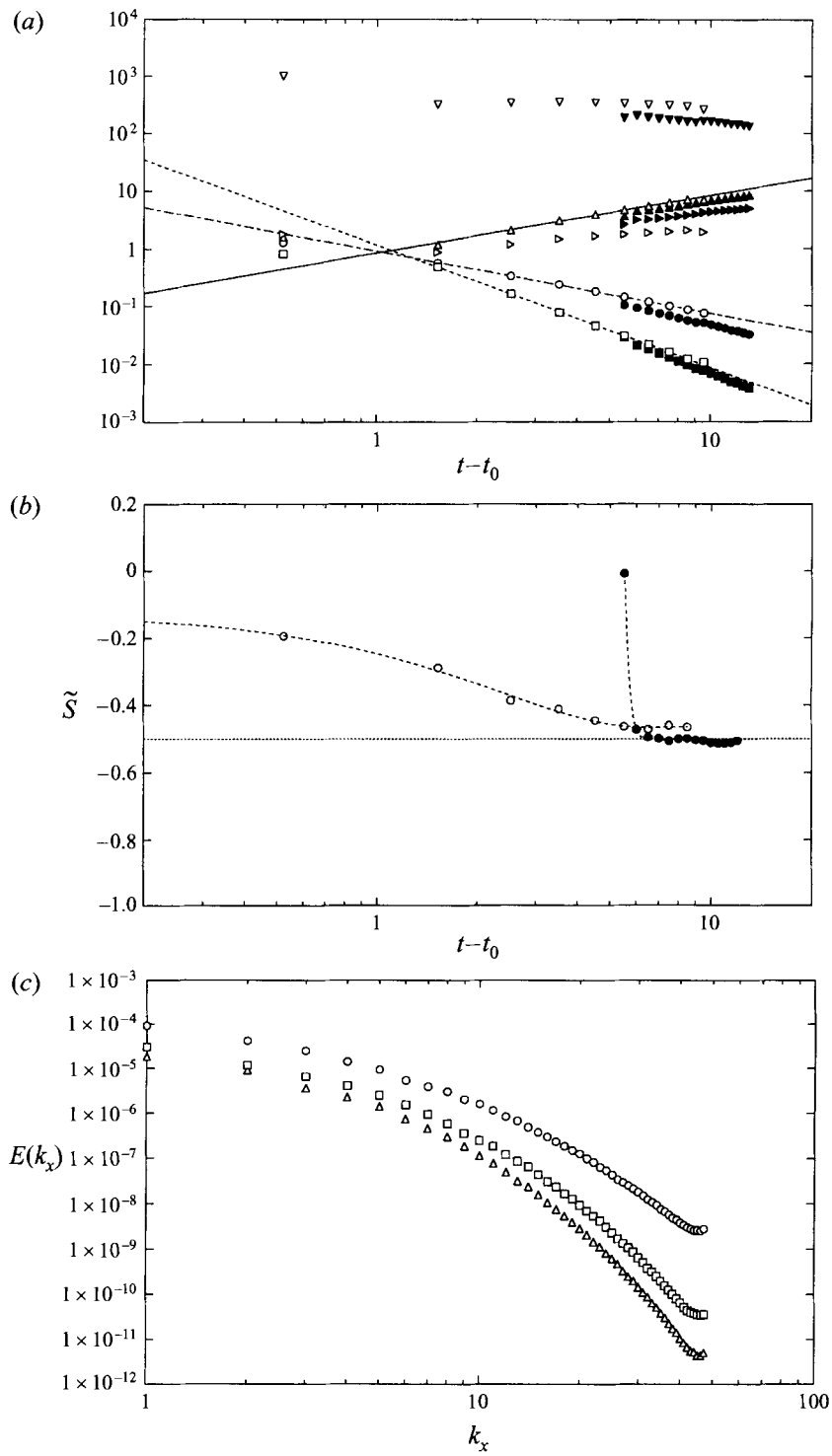

FIGURE 1. (*a*) Time evolution of various volume-averaged quantities: ○, $\tilde{k}$; □, $\tilde{\epsilon}$; △, $T=\tilde{k}/\tilde{\epsilon}$; ▷, L; ▽, Re_T; ——, $T=0.836(t-t_0)$, $R^2=0.998$; – – – –, $\tilde{k}=0.897(t-t_0)^{-1.088}$, $R^2=1.000$; – – – –, $\tilde{\epsilon}=1.146(t-t_0)^{-2.127}$, $R^2=1.000$. (*b*) Time evolution of the volume-averaged velocity-derivative skewness. Solid symbols in (*a*) and (*b*) indicate evolution after randomization. (*c*) The one-dimensional energy spectrum at various times: ○, $t=5$; □, $t=10$; △, $t=13$.

The same random multiplier is used at all z-locations to ensure that the boundary conditions are satisfied by the new velocity field:

$$\hat{v}_{new}(k_x, k_y, z) = \hat{v}_{old}(k_x, k_y, z)/r(k_x, k_y), \tag{4}$$

where r is a complex random number. The new 'randomized' velocity field is statistically independent of the initial generating field, but retains the spectrum of the generating field. These sixteen separate flows were then allowed to evolve for an additional five time units before the statistics were calculated.

2.3. *Turbulence decay*

Comparing the rate of decay of the simulated turbulent flow to recent theoretical predictions will verify that the isotropic region of the flow is self-preserving in character. Speziale & Bernard (1992), in studying the decay of self-preserving turbulence, developed an evolution equation for the turbulent Reynolds number and evaluated the fixed points of that equation. Two stable solutions exist depending on the initial palinstrophy coefficient G defined as:

$$G = \frac{30}{7} \frac{\nu \overline{\dfrac{\partial \omega_i}{\partial x_j} \dfrac{\partial \omega_i}{\partial x_j}} \Big/ \overline{\omega_k \omega_k}}{\epsilon/k}, \tag{5}$$

which is, as they noted, the ratio of turbulent to dissipative timescales. Their analysis indicated that for $G > \frac{30}{7}$ the turbulent Reynolds number

$$Re_T = k^2/\nu\epsilon \tag{6}$$

would approach a non-zero constant. If $G \leqslant \frac{30}{7}$ the solution is $Re_T = 0$. The two solutions also have different rates of decay of kinetic energy $k \sim t^{-\alpha}$: For the low-Reynolds-number solutions, $\alpha = \frac{5}{2}$ is the rate of decay, while for the high-Reynolds-number solution they find $\alpha = 1$.

For comparison, the temporal behaviour of several volume-averaged parameters are shown in figure 1(*a*). These include the volume-averaged turbulence kinetic energy $\tilde{k}$, the volume-averaged dissipation rate $\tilde{\epsilon}$, turbulent (or large-eddy) timescale $T = \tilde{k}/\tilde{\epsilon}$, and the turbulent lengthscale L. Data are presented for both the initial simulation (open symbols) and the simulations using the velocity field randomized at five computational time units (solid symbols). The time is normalized with the initial integral scale of the turbulence and the initial r.m.s. velocity, and $t = 0$ is the time of boundary insertion. The origin of time has been shifted by an amount $t_0 = 0.476$ (this offset was chosen so that T increases linearly with time, as required by its definition). For the initial simulation, Re_T is roughly constant. For the randomized flows, Re_T has decreased to approximately 147 and exhibits a weak decay. Also shown is the decay of turbulence kinetic energy. A least-squares fit of the rate of decay yields $\alpha = 1.088$, very close to the constant-Reynolds-number, self-preserving fixed point solution determined by Speziale & Bernard (1992). There is a noticeable reduction in the kinetic energy immediately after randomization as the flow responds to the perturbation. The initial vale of Re_T, L and T are likewise shifted after randomization due to the reduction in $\tilde{k}$. After these transients, the temporal behaviour is the same as the unperturbed flow. This comparison indicates that the simulation behaves in a manner consistent with high-Reynolds-number self-preserving turbulence, even though the free-surface boundaries are present.

Whether the turbulence decays in a self-similar fashion (Re_T = constant) or decays to zero, depends on the value of the palinstrophy coefficient. In this ensemble of simulations, during the time period for which statistics presented below were calculated, $Re_T = 147$ and $\tilde{G} = 5.44$, where $\tilde{G}$ is the palinstrophy coefficient averaged over the entire volume. This is larger than the critical value of $\frac{30}{7}$ and indicates that the turbulence, in the absence of boundaries, would be self-preserving during this period.

Another indicator of the self-preserving decay is the velocity-derivative skewness factor

$$S = \frac{\overline{(\partial u/\partial x)^3}}{\overline{[(\partial u/\partial x)^2]^{3/2}}}. \tag{7}$$

The velocity derivative skewness of the initial and randomized flows are shown in figure 1(*b*). From the initial, unrandomized flow, it is apparent that the expected value of approximately 0.5 (Kerr 1985) is not reached until five computational time units have passed. For the randomized flows, the skewness converges quickly, possibly because the energy spectrum is not altered by the randomization process. For the period during which the statistics discussed below were calculated, the volume-averaged velocity-derivative skewness factor was $\tilde{S} = 0.501$, again consistent with the behaviour of high-Reynolds-number homogeneous isotropic turbulence. Betchov (1956) showed a connection between the skewness and the production of enstrophy. Since the skewness has converged to the expected value and is nearly constant, the proper production of enstrophy and nonlinear energy transfer has been re-established after the flow randomization.

The one-dimensional energy spectrum, presented in figure 1(*c*), provides an indication of the adequacy of the spatial resolution of the simulation. The spectrum is shown for times $t = 5$, 10 and 13. The results for $t = 5$ are prior to randomization of the flow, while the statistics presented below were calculated for roughly $10 \leqslant t \leqslant 13$. At $t = 5$, the spectrum has a range of nearly five decades in energy between the low- and high-wavenumber limits, indicating a well-resolved flow. At $t = 10$, the range has increased to about six decades and at $t = 13$ the resolution has increased further.

2.4. *Scaling*

For the flow examined here, a consequence of the nearly self-similar decay is the similarity of the temporal behaviour of the turbulent, or large-eddy, lengthscale L, the Kolmogorov lengthscale $\eta = (\nu^3/\epsilon)^{1/4}$, and the viscous lengthscale $(\nu t)^{1/2}$. The viscous lengthscale will in all cases increase in proportion to $t^{1/2}$. For the exact self-similar decay of Speziale & Bernard (1992) (i.e. $\alpha = 1$), $L \sim t^{1/2}$ and $\eta \sim t^{1/2}$ as well. For the present simulations $\alpha = 1.088$, but the temporal behaviour of the turbulent and Kolmogorov lengthscales are only slightly different from that of the viscous lengthscale: $L \sim t^{0.46}$ and $\eta \sim t^{0.52}$. Similar results are obtained for the various timescales; for exact self-similar decay, the various timescales increase in proportion to t.

The above arguments can be extended to the boundary, at least for the tangential velocity. Kambe (1984) used an exact solution to the Navier–Stokes equations as a model for the interaction of two vortex rings in an axisymmetric collision. The plane of symmetry equidistant between the rings is similar to the shear-free free surface under consideration. Kambe showed that the lengthscale normal to the interface for the tangential velocity variations is $l \sim (\nu/s)^{1/2}$ where s is the rate of strain acting on the vortex. Regardless of the scaling assumed for s, we arrive at $l \sim t^{1/2}$ which is consistent with any of the three possible length scalings.

As a result of the foregoing, we conclude that for the flow examined here, which decays in a nearly self-similar fashion, all candidate scalings for any of the phenomena observed are nearly equivalent, and no conclusions can be drawn relative to the appropriateness of one or the other scaling. We therefore use the turbulent, or large-eddy, lengthscale L exclusively in non-dimensionalizing distance from the free surface since, for the flow in question, this choice is as good as any other. This is not meant to imply that in other flows, undergoing non-self-similar decay (i.e. Perot & Moin 1995), other scalings might not appear to be more useful.

2.5. *Calculation of statistical quantities*

The flow examined in this study is non-stationary and homogeneous only in planes parallel to the free surface. The statistics are, however, invariant under rotation in planes parallel to the free surface, and under reflection about planes normal to the free surface. The statistics are also invariant under reflection about the midplane of the computational domain (parallel to the free surface).

For a given instant in time, statistical quantities were calculated by first averaging over planes parallel to the free surface. Secondly, the symmetry about the midplane of the computational domain was exploited by averaging together data at equal distances from either free surface. Thirdly, the invariance under reflection about planes normal to the free surface was used; this ensured that the mean velocities were zero. Finally, the rotational invariance (about an axis normal to the free surface) was used, by averaging results for the two tangential velocity components together.

To improve convergence of the statistical quantities, the results from the entire ensemble were averaged over a short period of time. The averaging time was three and a half computational time units, which is equivalent to roughly half the large-eddy timescale (eddy 'turn-over' time) $T = \tilde{\epsilon}/\tilde{k}$ at the time period in question. Based on an initial eddy 'turn-over' time T_0, defined at $t - t_0 = 1$ (see figure 1*a*), the averaging begins at $t = 10T_0$ and the data is averaged for $3.5T_0$.

3. Results

In the results presented below, mean quantities are indicated by an overbar ($\overline{u^2w}$), and root-mean-square (r.m.s.) quantities are designated using a prime (u', w'). In these results, x and y are the coordinates parallel (tangential) to the free surface and the respective velocities are u and v. Since the turbulence statistics are invariant under rotation in planes parallel to the free surface, the x- and y-directions are indistinguishable. Therefore, unless otherwise noted, the x-component will be used to refer collectively to both tangential directions. The surface-normal direction is defined as the z-direction, positive downward, with the origin at the free surface. This will be referred to as the vertical direction with velocity component w.

In the profiles presented, the distance from the free surface is normalized with the turbulent lengthscale $L = \tilde{k}^{3/2}/\tilde{\epsilon}$, where $\tilde{k}$ and $\tilde{\epsilon}$ are the turbulence kinetic energy and dissipation rate averaged over the computational domain. (As noted above, different candidate scalings cannot be distinguished, and so this will be used consistently.) With this normalization, the computational domain is a cube which is $4.25L$ on a side, and the centreplane of the domain is at $z/L = 2.125$. As a result of the symmetry of the flow only the results for the upper half of the volume are shown. For this flow, $Re_T = 147$. In what follows, we present statistics related to the velocity, vorticity and pressure fields in §3.1. In §3.2, the various terms in the transport equations for the Reynolds stresses are then examined, followed by those for the turbulence kinetic energy equation. Terms

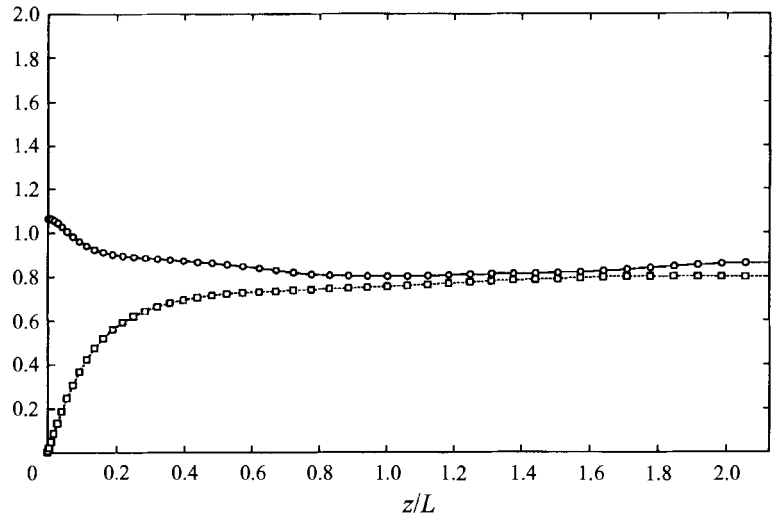

FIGURE 2. Profiles of r.m.s. velocity normalized with $\tilde{k}^{1/2}$; ○, u'; □, w'.

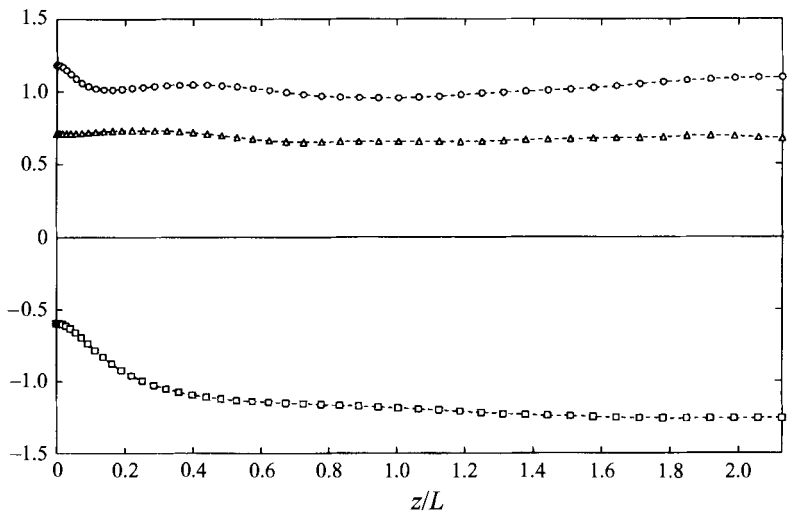

FIGURE 3. Profiles of turbulence kinetic energy and pressure-related quantities normalized with $\tilde{k}$; ○, k; □, $\bar{P}/\rho$; △, p'/ρ.

in the transport equations for the enstrophy and its component vorticity fluctuations are presented in §3.3.

3.1. *Statistical quantities*

3.1.1. *Velocity field*

Figure 2 shows the r.m.s. velocities as a function of the vertical distance from the free surface. The r.m.s. velocities are normalized with $\tilde{k}^{1/2}$. For $z/L \geqslant 1.0$, u' and w' are equal to within 5% r.m.s. The vertical component w' is consistently lower than the tangential component u'. This is the effect of the larger decay rate for $\overline{w^2}$ near the surface and is discussed below in §3.2.2. As the free surface is approached, two distinct regions are evident in u'. First, u' gradually increases over the region $0.1 \leqslant z/L \leqslant 1.0$.

There is a sharper rise near the free surface ($z/L \leqslant 0.1$). Over the range $0 \leqslant z/L \leqslant 1.0$, there is a smooth decrease in w' to zero at the free surface. The slope of the w' profile increases as the surface is approached.

The r.m.s. velocities are not perfectly constant in the centre portion of the computational domain, but vary slightly. This is due mainly to the confinement of the turbulence between the two free surfaces in the computational domain. These variations are small and are judged to be acceptable; however, their effect will be seen in other statistical quantities presented below, particularly in the turbulent transport terms in the Reynolds-stress transport equations.

The turbulence kinetic energy k normalized with $\tilde{k}$ is shown in figure 3. The level of k is roughly equal to $\tilde{k}$ over the entire domain, but rises slightly near the centreplane. There is a sharp increase of 15% near the free surface ($z/L \leqslant 0.1$) which corresponds to the increase in u'. This increase can be related to the local reduction in dissipation which is caused by the requirement that the tangential vorticity vanish at the free surface, and will be discussed below.

The anisotropy of the Reynolds stress describes the partitioning of energy among the fluctuating velocity components. It is also often used in the modelling of turbulence. The anisotropy tensor a_{ij} is defined by Newman & Lumley (1977) as

$$a_{ij} = \frac{\overline{u_i u_j} - \frac{2}{3}\delta_{ij} k}{k}. \tag{8}$$

For isotropic turbulence, $a_{ij} = 0$. Figure 4(*a*) shows the anisotropy for the tangential velocity fluctuations a_{uu}. (The anisotropy for the surface-normal fluctuations is $a_{ww} = -2a_{uu}$.) Far from the surface, the anisotropy is slightly non-zero, owing to the small difference between u' and w'. For $z/L \leqslant 1$, the anisotropy increases as the free surface is approached, reaching the limiting value of $\frac{1}{3}$ at the surface. Except for very near the surface, the slope of a_{uu} increases as the free surface is approached and two regions are again evident – a region of slow increase for $0.2 \leqslant z/L \leqslant 1$, and a region of more rapid increase for $z/L \leqslant 0.2$. In the combination of u' and w' embodied in the anisotropy a_{uu} the region of sharp increase in u' and k ($z/L \leqslant 0.1$) is not in evidence; there is now a broader region of rapid increase, $z/L \leqslant 0.2$, which is a result of the smoother behaviour of the w' velocity.

The invariants of the anisotropy tensor a_{ij} can be used to examine the nature of the turbulence as it approaches the free surface. Since a_{ij} has zero trace (by definition), the second and third invariants are all that are required. The second invariant is defined as

$$A_2 = a_{ij} a_{ji} \tag{9}$$

and is positive definite. In homogeneous, isotropic turbulence, it is zero, and when one r.m.s. velocity vanishes and the other two are equal (as occurs at the free surface), it has a value of $\frac{2}{3}$. The third invariant of a_{ij} is

$$A_3 = a_{ij} a_{jk} a_{ki}. \tag{10}$$

A_3 is negative for the case of two equal r.m.s. velocities which are larger than the third, with a limiting value of $-\frac{2}{9}$ when the third component vanishes.

Plots of these invariants versus distance from the free surface are shown in figure 4(*b*). Far from the surface $z/L > 1$, both invariants are zero, indicating nearly isotropic behaviour. The second invariant A_2 captures the gradual increase in anisotropy for

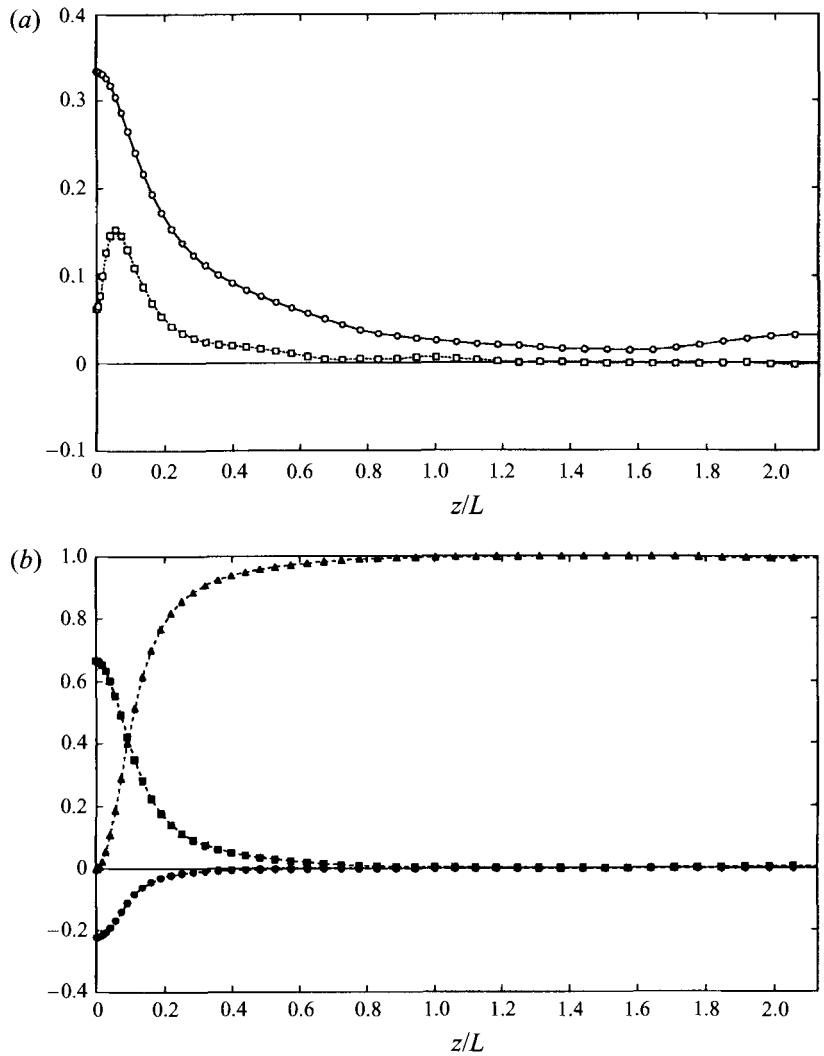

FIGURE 4. Profiles of Reynolds-stress and dissipation anisotropy and invariants of the Reynolds stress anisotropy tensor: (*a*) Reynolds-stress and dissipation anisotropy; ○, $a_{uu} = -2a_{ww}$; □, $e_{uu} = -2e_{ww}$; (*b*) invariants of the Reynolds stress anisotropy tensor; ■, A_2; ●, A_3; ▲, $1-\frac{9}{8}(A_2-A_3)$ ('flatness' factor).

$0.2 \leqslant z/L \leqslant 1$ and the sharp increase for $z/L \leqslant 0.2$. The third invariant A_3 appears to capture primarily the sharp increase in anisotropy for $z/L \leqslant 0.2$. Both invariants attain their respective limiting values at the surface. Also shown in figure 4(*b*) is a 'flatness' factor often used in turbulence modelling to capture anisotropic behaviour (see e.g. Launder 1990). This factor is defined as $1-\frac{9}{8}(A_2-A_3)$. Since, at the surface, $A_2-A_3 = \frac{8}{9}$ and, far from the surface, A_2 and A_3 are both zero, the flatness factor will vary from zero at the surface to unity far from the surface in a manner which reflects the anisotropy of the turbulence. This factor is equal to one for $z/L \geqslant 1.0$ and exhibits the same two regions seen in A_2 and a_{uu}. In using these invariants to control the modelling of near-surface effects, it is clear that the 'flatness' factor reflects the anisotropy which exists at all the locations; A_2 does this somewhat less well, while A_3 reflects mainly the 'strong' anisotropy which exists for $z/L \leqslant 0.2$.

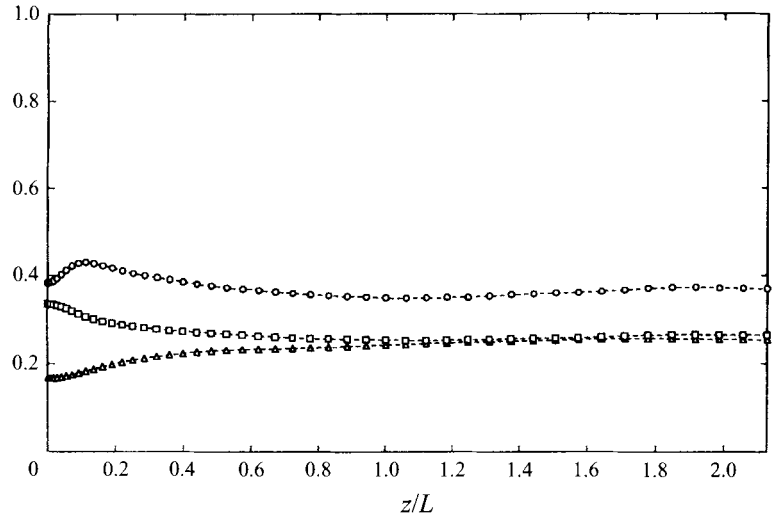

FIGURE 5. Profiles of the Taylor microscales, normalized with L; ○, λ_f, the longitudinal microscale; □, λ_{gv}, the lateral microscale associated with the v velocity; △, λ_{gw}, the lateral microscale associated with the w velocity.

3.1.2. *Lengthscales*

The Taylor microscale can be defined as

$$\lambda_i = \left(\frac{2\overline{u_i^2}}{\overline{(\partial u_i/\partial x_j)^2}} \right)^{1/2}, \tag{11}$$

where there is no summation on repeated indices (see e.g. Hinze 1975, p. 41). Here, x_j denotes a direction in which the turbulence is homogeneous (the surface-parallel direction x for the flow in question) and u_i can be any component of the velocity. For $i = j$, the longitudinal correlation λ_f is obtained. For $i \neq j$, the lateral correlations associated with the surface-normal and surface parallel velocities, λ_{gw} and λ_{gv}, respectively, are obtained. These scales represent the scale on which longitudinal straining occurs (λ_f) and the scales associated with the normal and tangential components of vorticity (λ_{gv} and λ_{gw}, respectively).

Figure 5 shows profiles of all three lengthscales normalized with L. Far from the free surface, the two lateral microscales, λ_{gv} and λ_{gw}, are equal and the longitudinal microscale λ_f is consistently larger, as would be expected in homogeneous isotropic turbulence. (For homogeneous isotropic turbulence, $\lambda_f = \sqrt{2}\lambda_g$; Hinze 1975, p. 188.) As the free surface is approached, λ_f increases by 10–15% to a maximum at $z/L \approx 0.1$. This is due to the increase in $\overline{u^2}$ near the boundary. For $z/L \leqslant 0.1$, λ_f decreases. Since $\overline{u^2}$ increases in this region, this indicates that the extensional strain $\partial u/\partial x$ has increased significantly near the surface. The lateral microscale associated with the w velocity λ_{gw} decreases by roughly 30% as the surface is approached. While both $\overline{w^2}$ and the fluctuating $\partial w/\partial x$ velocity gradient go to zero at the surface, the associated lengthscale remains finite. The lateral microscale associated with v, λ_{gv}, increases by about 30% at the boundary. This is mainly due to the increase in the tangential velocity fluctuations.

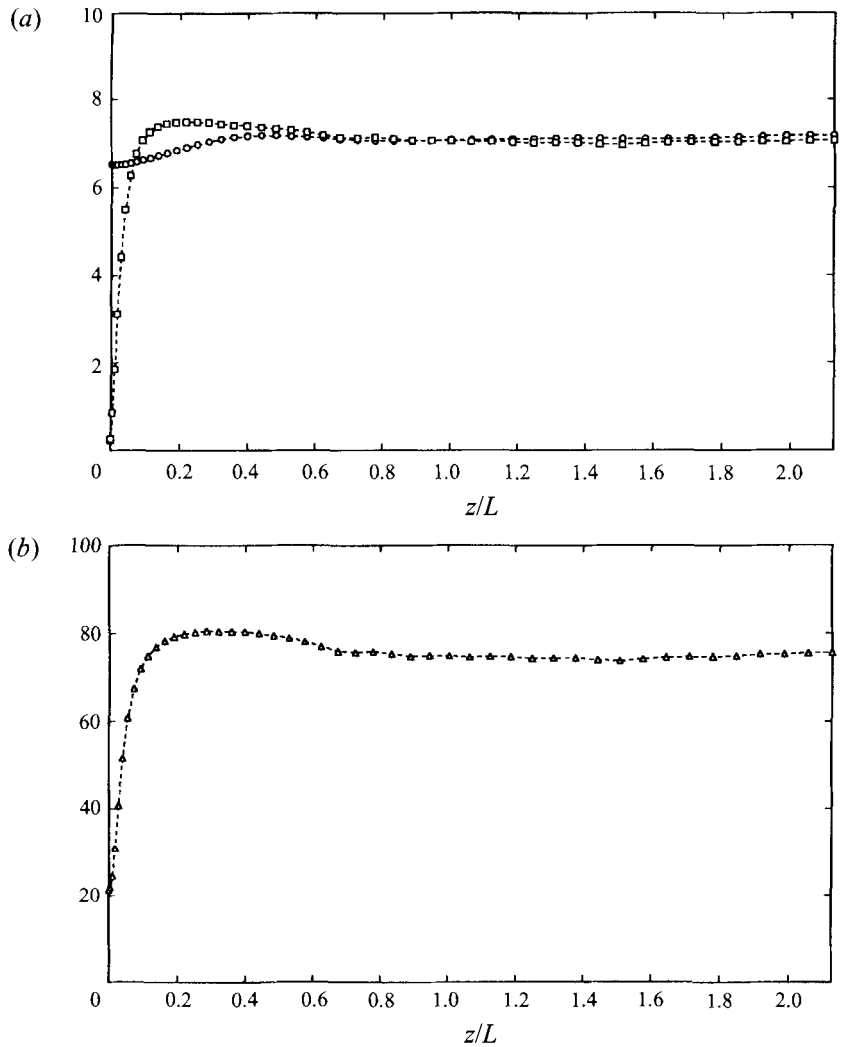

FIGURE 6. Profiles of r.m.s. vorticity and enstrophy; (*a*) r.m.s. vorticity normalized with $\tilde{\epsilon}/\tilde{k}$; □, ω_x'; ○, ω_z'; (*b*) enstrophy $\frac{1}{2}\overline{\omega_i\omega_i}$ normalized with $\tilde{\epsilon}^2/\tilde{k}^2$.

3.1.3. *Vorticity field*

The root-mean-square vorticity is shown in figure 6(*a*). The vorticity is normalized by the inverse of the turbulent timescale $\tilde{\epsilon}/\tilde{k}$. The tangential component, ω_x', is zero at the free surface, owing to the imposed boundary conditions. The level of ω_x' rises sharply over the range $0 \leqslant z/L \leqslant 0.10$ and peaks at $z/L = 0.2$ before decreasing slightly and becoming constant for $z/L \geqslant 0.8$. The region of increase is roughly half a lateral microscale thick. The r.m.s. surface-normal vorticity ω_z' is also shown in figure 5. This component is constant for $z/L \geqslant 0.4$ (and is equal to ω_x' for $z/L \geqslant 0.8$) but decreases by 10% as the free surface is approached.

The enstrophy, defined as $\frac{1}{2}\overline{\omega_i\omega_i}$, is shown in figure 6(*b*), where it has been normalized by the $(\tilde{\epsilon}/\tilde{k})^2$. The enstrophy has a minimum at the free surface and rises sharply over the region $z/L \leqslant 0.10$. There is a broad maximum at $z/L \approx 0.28$, followed by a small decrease (5–10%); the enstrophy then becomes constant for $z/L \geqslant 0.8$.

The Reynolds stress term appearing in the Reynolds-averaged form of the

Navier–Stokes momentum equations (the RANS equations) can be written in rotational form (Hinze 1975, p. 568)

$$-\frac{\partial \overline{u_j u_i}}{\partial x_j} = \epsilon_{ijk}\overline{u_j \omega_k} - \frac{\partial}{\partial x_i}\frac{\overline{u_j u_j}}{2}$$

$$= \epsilon_{ijk}\overline{u_j \omega_k} - \frac{\partial k}{\partial x_i}, \tag{12}$$

where ω_i is the fluctuating vorticity. (Here, ϵ_{ijk} is the alternating unit tensor, used to form the vector cross-product between the fluctuating velocity and vorticity.) The second term on the right of (12) is the gradient of the dynamic pressure associated with the turbulent fluctuations – the turbulence kinetic energy. The first term on the right-hand side of (12) is a non-potential body force resulting from translation of a material particle in a direction normal to the local vorticity vector; the resultant body force is normal to both the vorticity and the direction of translation – a 'lift' force acting on the fluid.

For homogeneous isotropic turbulence, the vorticity and velocity will be uncorrelated. Even in more complex flows, the vorticity and velocity fluctuations remain only weakly correlated since the lengthscales for the vorticity fluctuations are typically much smaller than those for the velocity fluctuations (see Tennekes & Lumley 1972, p. 81). A boundary such as a free surface can cause the vorticity and velocity fluctuations to become correlated. The requirement that w vanish at the surface causes the surface-parallel vorticity component at a point to induce a local surface-parallel velocity which is normal to the local vorticity vector. This velocity is such that the local value of the associated velocity–vorticity correlation term ($\epsilon_{ijk}\overline{u_j \omega_k} = \overline{u\omega_y} - \overline{v\omega_x}$) will be negative for z positive downward (see Walker *et al.* 1995). At the free surface, the correlations must vanish since the tangential vorticity does. For large distances from the surface, the induced velocity will be reduced (for a potential vortex, it would decrease roughly as z^{-1}). Hence, near a free surface one would expect to find a negative peak in the correlation between orthogonal components of the tangential velocity and tangential vorticity. Significant correlation between the fluctuating velocity and vorticity indicates that the interaction of the vorticity with the free surface is sufficient to affect the Reynolds stress field.

Figure 7 shows the velocity–vorticity correlation $\overline{u\omega_y}$ for this flow. The correlation is negligibly small over the centre 50% of the computational domain and becomes negative near the free surface. At the free surface, $\overline{u\omega_y}$ is zero. It then rises sharply in magnitude to a peak at $z/L \approx 0.05$ and drops slowly to near zero at $z/L \approx 1.0$. Also shown in figure 7 is the correlation coefficient for the velocity–vorticity correlation

$$R_{u\omega} = \frac{\overline{u\omega_y}}{u'\omega_y'}. \tag{13}$$

The correlation between the velocity and vorticity fluctuations has a maximum of $R_{u\omega} = 0.3$ at $z/L \approx 0.04$. This level remains relatively constant over the near-surface region where the pronounced drop in ω_x' occurs, and then decreases to zero at the free surface. This indicates that the decrease in the velocity–vorticity correlation can be attributed to the decrease in ω_y' which occurs as a result of the no-shear condition at the free surface. Except for very near the surface, the degree of correlation increases as the surface is approached, as would be expected for vorticity interacting with a $w = 0$ boundary. This significant degree of correlation indicates that vorticity/free-surface interaction modifies the Reynolds stress field near the surface.

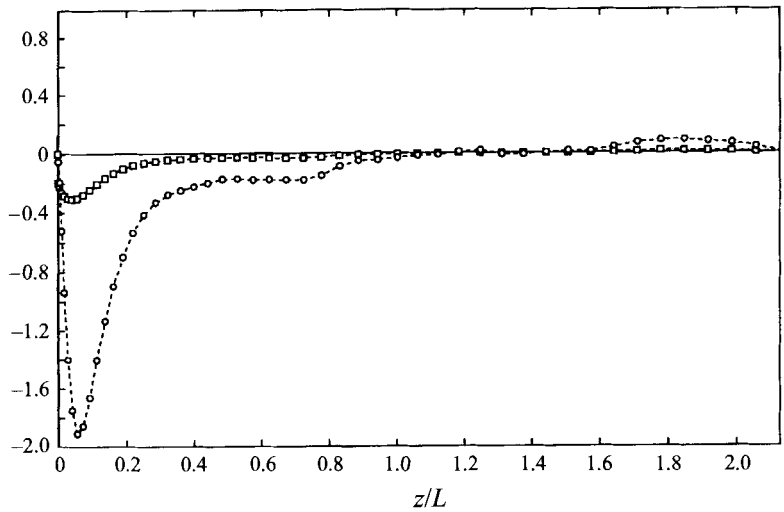

FIGURE 7. Profiles of velocity–vorticity correlations normalized with $\tilde{\epsilon}/\tilde{k}^{1/2}$ and correlation coefficient, ○, $\overline{u\omega_y}$; □, $R_{uw} = \overline{u\omega_y}/u'\omega_y'$.

3.1.4. *Pressure field*

The pressure field near the surface is very important in free-surface flows. Not only does the pressure contribute to transport of turbulent stress and redistribution of energy, but, in non-zero-Froude-number flows, it generates surface waves. Here we examine the mean and r.m.s. pressure and formulate the Poisson equation which governs the pressure field. Examination of these gives an indication of the types of motions in the flow which result in the observed pressure field.

Figure 3 shows the mean pressure $\bar{P}/\rho$ and root-mean-square pressure p'/ρ, both normalized with $\tilde{k}$. (The pressure is the only quantity in this flow for which the mean is non-zero. Therefore we will use P to denote the instantaneous pressure, $\bar{P}$ to denote the mean pressure, and p to denote fluctuations relative to the mean.) The mean pressure $\bar{P}/\rho$, which is related to $\overline{w^2}$ through the mean vertical momentum equation, mirrors the behaviour of $\overline{w^2}$. It is relatively constant over the centre portion of the flow, and rises for $z/L \leqslant 0.5$. The rise near the surface is about $0.5\,\tilde{k}$. The r.m.s. pressure is relatively constant at about $0.7\,\tilde{k}$.

The observed behaviour in the pressure field near the surface can be explained by examining the governing Poisson equation for the pressure. This equation is obtained by taking the divergence of the Navier–Stokes equations. This procedure results in:

$$\frac{\partial^2}{\partial x_i^2}\frac{P}{\rho} = -\frac{\partial u_j}{\partial x_i}\frac{\partial u_i}{\partial x_j} = -f(x_i). \tag{14}$$

Each velocity gradient term on the right-hand side of (14) can be decomposed into symmetric and anti-symmetric parts (irrotational strain and rotation). After some manipulation, the resulting equation is

$$\frac{\partial^2}{\partial x_i^2}\frac{P}{\rho} = -(S_{ij}S_{ji} - \tfrac{1}{2}\omega_i\omega_i), \tag{15}$$

where

$$S_{ij} = \frac{1}{2}\left(\frac{\partial u_i}{\partial x_j} + \frac{\partial u_j}{\partial x_i}\right) \tag{16}$$

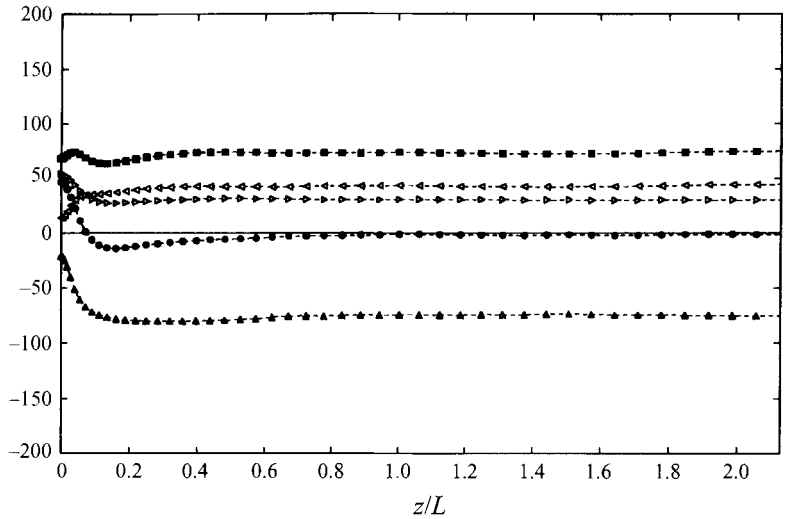

FIGURE 8. Source terms in the Poisson equation for the mean pressure, normalized with $\tilde{\epsilon}^2/\tilde{k}^2$; ●, $\bar{f} = \overline{S_{ij}S_{ji}} - \frac{1}{2}\overline{\omega_i\omega_i}$; ■, $\overline{S_{ij}S_{ji}}$. ▲, $-\frac{1}{2}\overline{\omega_i\omega_i}$; ▷, normal-strain component of $\overline{S_{ij}S_{ji}}$; ◁, shear-strain component of $\overline{S_{ij}S_{ji}}$.

is the irrotational strain-rate tensor. The two source terms on the right-hand side of (15) are, respectively, the second invariant of S_{ij}, a measure of the magnitude of the instantaneous irrotational strain field, and the enstrophy, a measure of the magnitude of the instantaneous rotation at a point. Equations (14) and (15) can be inverted to yield expressions for the pressure field in terms of a weighed volume integral of the source terms (Greenberg 1971, p. 112). The appropriate solution is

$$\frac{P(x_i)}{\rho} = \int_V G(x_i, x_i') f(x_i')\,\mathrm{d}x_i'^3$$

$$= \int_V G(x_i, x_i')\,(S_{ij}S_{ji} - \tfrac{1}{2}\omega_i\omega_i)\,\mathrm{d}x_i'^3, \tag{17}$$

where

$$G(x_i, x_i') = \frac{1}{4\pi}\left(\frac{1}{|x_i' - x_i|} + \frac{1}{|x_i'^* - x_i|}\right) \tag{18}$$

is the Green's function. Here, the second term in (18) represents integration over the velocity field reflected in the plane of the free surface, and is included to satisfy the condition $\partial P/\partial z = 0$ at $z = 0$. Taken together, (17) and (18) indicate that the pressure at a point is influenced by the entire velocity field, but mainly depends on the magnitude of the source term f in the immediate vicinity of that point. Hence, by examining f we can gain some insight into the mechanisms which influence the pressure field in this flow. In the decomposition of the source term shown in the second line of (17), both of the terms are positive definite and so (17) indicates that an instantaneous increase in the strain rate will cause an increase in the pressure, while an instantaneous increase in the enstrophy will cause a decrease in P.

If we average (17) we can see that the mean pressure is determined by the means of the source terms. Figure 8 shows the local mean value of the source terms from (17) versus distance from the surface. The mean of the entire source term $\bar{f}$ is constant and near zero for $z/L \geqslant 0.5$. As the surface is approached, $\bar{f}$ first decreases slightly and then rises sharply for $z/L \leqslant 0.1$. The rise in $\bar{f}$ near the surface is responsible for the increase

in the mean pressure there. Comparison to the mean pressure (figure 3) shows that the influence of the rise in $\bar{f}$ near the surface affects the entire near-surface region, out to $z/L \approx 0.4$ and beyond, owing to the Green's function in (17). Figure 8 also shows the means of the terms which comprise f. The first term $\overline{S_{ij}S_{ji}}$ is relatively constant for $z/L \geqslant 0.5$, and varies only slightly as the surface is approached. This term can be decomposed into contributions from fluctuations in the shear strain rate, the portion of $\overline{S_{ij}S_{ji}}$ for $i \neq j$, and fluctuations in the normal strain rate, the portion for which $i = j$. Near the surface, large normal strain rates result from stagnation-type flow ('splats' or 'anti-splats', in the parlance of Bradshaw & Koh 1981 and Perot & Moin 1993), a consequence of the $w = 0$ condition at the surface. The fluctuations in the shear strain rate can be expected to decrease near the surface owing to the no-shear condition. These effects roughly offset each other and, as a result, there is no net change in the mean pressure resulting from the irrotational strain. The second term $-\frac{1}{2}\overline{\omega_i\omega_i}$ is equal in magnitude to $\overline{S_{ij}S_{ji}}$ for $z/L \geqslant 0.5$, but increases sharply for $z/L \leqslant 0.1$. This reduction in the fluctuating enstrophy, a change in the rotational part of the flow, is responsible for the observed increase in the mean pressure at the free surface.

3.2. *Reynolds-stress and turbulence-kinetic-energy balances*

Transport equations for the elements of the Reynolds stress tensor $\overline{u_iu_j}$ can be derived from the Navier–Stokes equations (see e.g. Hinze 1975, p. 323). For a flow with zero mean velocity the equations have the following form

$$\underbrace{\frac{\partial}{\partial t}\overline{u_iu_j}}_{\text{I}} = \underbrace{-\frac{\partial}{\partial x_k}\overline{u_iu_ju_k} - \frac{1}{\rho}\left(\frac{\partial}{\partial x_i}\overline{pu_j} + \frac{\partial}{\partial x_j}\overline{pu_i}\right)}_{\text{II}} + \underbrace{\frac{1}{\rho}\overline{p\left(\frac{\partial u_j}{\partial x_i} + \frac{\partial u_i}{\partial x_j}\right)}}_{\text{III}} \underbrace{- 2\nu\overline{\frac{\partial u_i}{\partial x_k}\frac{\partial u_j}{\partial x_k}}}_{\text{IV}} + \underbrace{\nu\frac{\partial^2\overline{u_iu_j}}{\partial x_k\partial x_k}}_{\text{V}}, \tag{19}$$

where term I represents time-rate-of-change of $\overline{u_iu_j}$ at a point in the flow, II represents transport of $\overline{u_iu_j}$ due to turbulent velocity and pressure fluctuations, III (the pressure–strain correlation) represents inter-component energy redistribution due to interactions between the fluctuating pressure and strain fields, IV represents loss of $\overline{u_iu_j}$ due to viscous dissipation, and V represents viscous diffusion of $\overline{u_iu_j}$. For the flow in question, which is homogeneous in planes parallel to the free surface, the mean gradients in the surface-parallel directions vanish and $\overline{u_iu_j} = 0$ for $i \neq j$. This results in the following equations for the non-zero Reynolds stresses. For the $\overline{u^2}$ Reynolds stress (involving surface-tangent velocities) (19) reduces to

$$\underbrace{\frac{\partial}{\partial t}\overline{u^2}}_{\text{I}} = \underbrace{-\frac{\partial}{\partial z}\overline{u^2w}}_{\text{II}} + \underbrace{\frac{2}{\rho}\overline{p\frac{\partial u}{\partial x}}}_{\text{III}} \underbrace{- 2\nu\overline{\left(\frac{\partial u}{\partial x_k}\right)^2}}_{\text{IV}} + \underbrace{\nu\frac{\partial^2}{\partial z^2}\overline{u^2}}_{\text{V}}, \tag{20}$$

and for the surface-normal velocity fluctuations, the $\overline{w^2}$ equation is

$$\underbrace{\frac{\partial}{\partial t}\overline{w^2}}_{\text{I}} = \underbrace{-\frac{\partial}{\partial z}\left(\overline{w^3} + \frac{2}{\rho}\overline{pw}\right)}_{\text{II}} + \underbrace{\frac{2}{\rho}\overline{p\frac{\partial w}{\partial z}}}_{\text{III}} \underbrace{- 2\nu\overline{\left(\frac{\partial w}{\partial x_k}\right)^2}}_{\text{IV}} + \underbrace{\nu\frac{\partial^2}{\partial z^2}\overline{w^2}}_{\text{V}}. \tag{21}$$

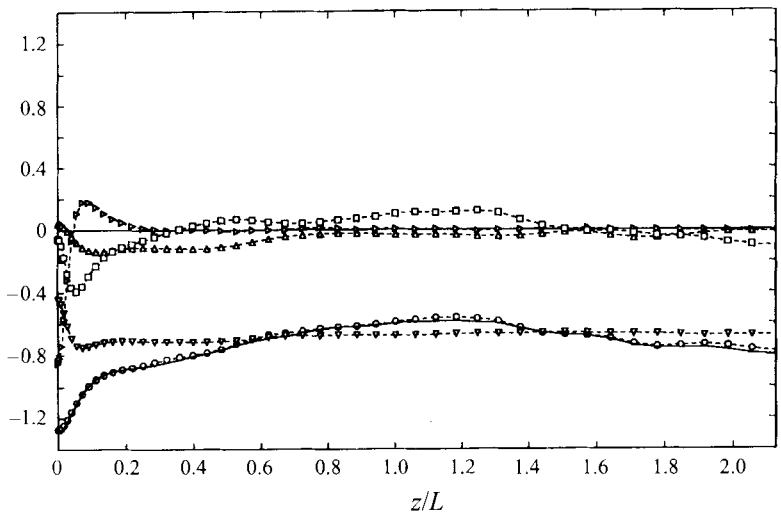

FIGURE 9. Terms in (20), the transport equation for the $\overline{u^2}$ Reynolds stress, normalized with ϵ; ○, time rate-of-change (term I); □, turbulent transport (term II); △, pressure–strain correlations (term III); ▽, dissipation (term IV); ▷, diffusion (term V); ——, sum of terms II–V.

Half the contraction of (19) is the turbulence kinetic energy equation

$$\underbrace{\frac{\partial k}{\partial t}}_{\text{I}} = \underbrace{-\frac{\partial}{\partial z}\left(\overline{k'w}+\frac{1}{\rho}\overline{pw}\right)}_{\text{II}} + \underbrace{0}_{\text{III}} \underbrace{-\nu\overline{\frac{\partial u_i}{\partial x_k}\frac{\partial u_i}{\partial x_k}}}_{\text{IV}} + \underbrace{\nu\frac{\partial^2 k}{\partial z^2}}_{\text{V}}, \tag{22}$$

where $k' = \frac{1}{2}u_i u_i$. In this expression, the pressure–strain correlations vanish owing to their redistributive nature, but the interpretation of the other terms is unchanged.

In the following sections, the terms of the Reynolds-stress balances are normalized with the volume-averaged dissipation rate $\tilde{\epsilon}$. The terms are plotted against z/L. Since the flow is undergoing nearly self-similar decay (Speziale & Bernard 1992), the large eddy, viscous and Kolmogorov lengthscales all grow as $t^{1/2}$. As noted earlier, the similarity of the temporal behaviour of the various lengthscales precludes any determination regarding the appropriate lengthscale for use in normalization, and no assertions about the proper normalization are made.

3.2.1. *Terms of the Reynolds stress balance for* $\overline{u^2}$

The terms appearing in (20), the balance of the $\overline{u^2}$ Reynolds stress, are shown in figure 9. All terms are normalized with the volume-averaged dissipation rate $\tilde{\epsilon}$. The dominant term in this temporally decaying turbulence is term IV, loss due to viscous dissipation, which is relatively constant at 0.70–0.75 $\tilde{\epsilon}$ for $z/L \geqslant 0.2$. The loss due to dissipation decreases rapidly as the free surface is approached to a level of 0.45 $\tilde{\epsilon}$ at the free surface. Diffusive transport (term V) is very small for $z/L \geqslant 0.2$. For $z/L \leqslant 0.2$, there is a local gain in $\overline{u^2}$ through diffusion which increases to a peak of 0.2 $\tilde{\epsilon}$ at $z/L = 0.1$ followed by a sharp decline as the free surface is approached. Very near the surface, there is a loss of $\overline{u^2}$ through diffusion with the maximum loss occurring at the surface. This is nearly twice the loss of $\overline{u^2}$ owing to dissipation at the surface. This indicates that diffusion transports $\overline{u^2}$ from very near the surface to the region $z/L \leqslant 0.2$. Transport of $\overline{u^2}$ by turbulent velocity fluctuations (term II) causes a loss of

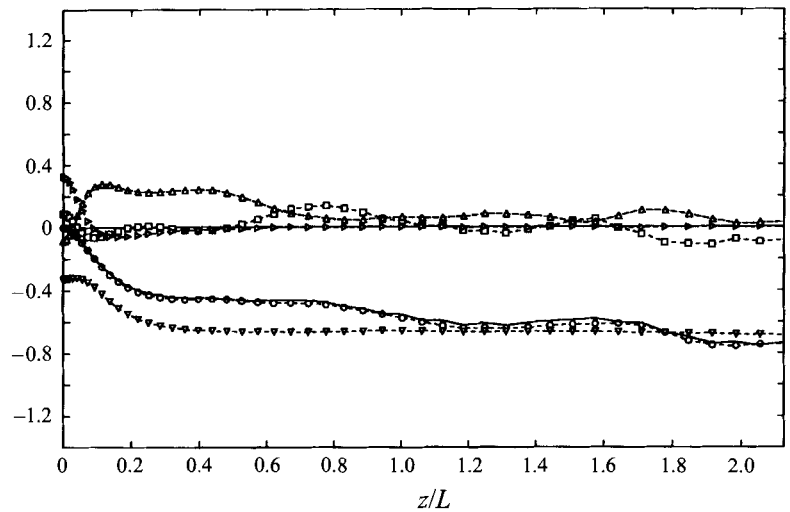

FIGURE 10. Terms in (21), the transport equation for the $\overline{w^2}$ Reynolds stress, normalized with $\tilde{\epsilon}$; ○, time rate-of-change (term I); □, turbulent transport (term II); △, pressure–strain correlations (term III); ▽, dissipation (term IV); ▷, diffusion (term V); ——, sum of terms II–V.

$\overline{u^2}$ from the near-surface region; the maximum loss is roughly 0.4 $\tilde{\epsilon}$ at $z/L = 0.06$. In general, the turbulent transport causes loss of $\overline{u^2}$ from regions where it is elevated, and gains where it is lower, relative to the surroundings. As a result, this quantity reflects the subtle variations in the u' profile seen in figure 1. Redistribution of energy from $\overline{w^2}$ to $\overline{u^2}$ (and *vice versa*) through interaction of the fluctuating pressure and strain fields is embodied in the pressure–strain correlations (term III). At the surface, there is a small positive contribution (0.05 $\tilde{\epsilon}$) to $\overline{u^2}$, indicating that transfer from $\overline{w^2}$ to $\overline{u^2}$ occurs at the surface. Further from the surface, down to $z/L \approx 0.7$, the pressure–strain correlation is consistently negative, with a broad maximum of roughly 0.1 $\tilde{\epsilon}$, more than twice the magnitude of the limiting value at the surface. In this deeper region the pressure–strain correlations serve to reduce the difference between $\overline{w^2}$ and $\overline{u^2}$ (i.e. they promote a 'return' to isotropy); whereas, in a small region at the surface they increase the difference. Far from the surface $z/L \geqslant 0.5$, the pressure–strain correlation is slightly negative, owing to the slight anisotropy in this region.

The sum of terms II–V, and the time derivative of $\overline{u^2}$ (term I), are also shown; these agree well across the entire flow. For $z/L \geqslant 0.6$, the time-rate-of-change for $\overline{u^2}$ is due primarily to viscous dissipation, with a small contribution from turbulent transport. For $z/L \leqslant 0.6$, the rate-of-change becomes more negative owing mainly to pressure–strain redistribution. Near the surface, losses due to diffusion and turbulent transport contribute to a rapid decrease near the surface, with diffusion dominating at the free surface.

3.2.2. *Terms of the Reynolds stress balance for* $\overline{w^2}$

The terms of the balance for the Reynolds stress associated with surface-normal velocity fluctuations $\overline{w^2}$ (equation (21)) are shown in figure 10, again normalized with $\tilde{\epsilon}$. As with $\overline{u^2}$, the balance of $\overline{w^2}$ is dominated by dissipation (term IV) for $z/L \geqslant 0.3$. The level of dissipation is similar to that for $\overline{u^2}$, 0.7 $\tilde{\epsilon}$. As the surface is approached, the dissipation rate decreases by 50% and is constant very near the surface. At the surface, the loss of $\overline{w^2}$ through dissipation is exactly balanced by gain due to diffusion; however, these two effects result in a net loss of $\overline{w^2}$ in the near-surface region. For $z/L \geqslant 0.10$,

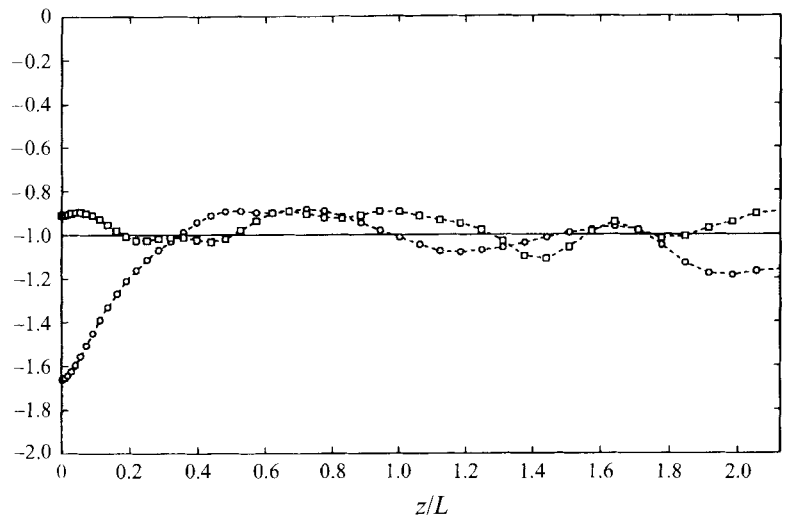

FIGURE 11. Inverse decay timescales for $\overline{u^2}$ and $\overline{w^2}$ normalized with $\tilde{\epsilon}/\tilde{k}$; □, $(\partial\overline{u^2}/\partial t)/\overline{u^2}$; ○, $(\partial\overline{w^2}/\partial t)/\overline{w^2}$.

there is no significant contribution to $\overline{w^2}$ owing to diffusion. Turbulent transport of $\overline{w^2}$ (term II) is small in magnitude, but makes a slight positive contribution near the surface, and a slight negative contribution farther from the surface. (Actually, the pressure transport and the transport due to velocity fluctuations roughly offset one another for $z/L \leqslant 0.2$. The latter causes a gain in $\overline{w^2}$ while the former results in a decrease – each with a magnitude of 0.35–0.40 at $z/L \approx 0.1$). The pressure–strain correlation term (III) is twice that for $\overline{u^2}$ and is of opposite sign, as expected. At the surface, there is a small loss of $\overline{w^2}$ resulting from transfer of energy to $\overline{u^2}$. Further from the surface, there is transfer of energy from $\overline{u^2}$ to $\overline{w^2}$, reflecting the anisotropy of the Reynolds stresses. The loss of $\overline{w^2}$ at the surface owing to pressure–strain redistribution is exactly balanced by the gain due to turbulent transport. This, coupled with the balance between dissipation and diffusion at the surface, results in zero net change in $\overline{w^2}$ at the surface. The time-rate-of-change (term I) increases in magnitude with increasing depth until it matches the dissipation rate for $z/L \geqslant 1.1$. Nearer the surface, the time-rate-of-change is less than the dissipation rate owing to contributions to $\overline{w^2}$ from the pressure–strain correlations.

These results are largely consistent with the results of Perot & Moin (1993). They showed that, near the surface, pressure transport and transport due to velocity fluctuations nearly balance, yielding little net turbulent transport. The pressure–strain term trend shown for early time ($t/T_0 < 3$) in Perot & Moin (1993) is consistent with the results in the present study ($t/T_0 > 10$). In their results, the pressure–strain correlation at the surface is negative and getting smaller in magnitude with increasing time. Further from the surface, there is a positive maximum which is increasing in time.

3.2.3. *Discussion of the Reynolds stress balances*

To gain further insight regarding the temporal decay of both Reynolds stresses, we can examine the time-rate-of-change of a given stress, normalized with the local value for the stress. This quantity can be thought of as a decay rate, or an inverse timescale, for the stress. The results for $\overline{u^2}$ and $\overline{w^2}$ are shown in figure 11, normalized with the inverse turbulent timescale $\tilde{\epsilon}/\tilde{k}$. Across the entire flow, the decay rate for $\overline{u^2}$ is roughly

constant and equal to $\tilde{\epsilon}/\tilde{k}$. This indicates that, for short times at least, the $\overline{u^2}$ profile will decrease in magnitude, but maintain its shape (i.e. it will exhibit self-similar behaviour). For $\overline{w^2}$, the decay rate is roughly equal to $\tilde{\epsilon}/\tilde{k}$ for $z/L \geqslant 0.4$, but for the region closer to the surface, the decay rate is larger, reaching at the surface a level more than 60% larger than $\tilde{\epsilon}/\tilde{k}$. This indicates that, far from the surface, $\overline{w^2}$ will decrease at the same rate as $\overline{u^2}$ but near the surface, $\overline{w^2}$ will decrease much more rapidly than $\overline{u^2}$.

The transport terms in (20) and (21), in large part, reflect the variations in the associated Reynolds stress; i.e. they respond to the changes in the stress profile caused by the boundary conditions or the action of the source terms. The source terms which affect the near-surface balance of the turbulent stresses are pressure–strain redistribution and viscous dissipation. Viscous dissipation decreases near the surface for both $\overline{u^2}$ and $\overline{w^2}$, but remains at finite levels. For $\overline{w^2}$, the fixed level of dissipation near the surface, where $\overline{w^2}$ decreases to zero, contributes to the large decay rates for this stress near the surface shown in figure 11. For $\overline{u^2}$, the reduced dissipation near the surface contributes to the observed increase in $\overline{u^2}$ near the surface.

The pressure–strain redistribution can be understood as follows: the primary effect of the surface, though the $w = 0$ condition, is to cause a transfer of energy from $\overline{w^2}$ to $\overline{u^2}$, via the pressure–strain correlations, as a result of the direct interaction of the flow with the boundary. However, pressure–strain redistribution of energy from $\overline{u^2}$ to $\overline{w^2}$ will occur if $\overline{u^2}$ is substantially larger than $\overline{w^2}$ (i.e. the transfer from $\overline{u^2}$ to $\overline{w^2}$ is driven by the local anisotropy; this is true anywhere in the flow, including near the free surface). Hence, there is a secondary effect of the boundary: the initial redistribution caused by the boundary increases $\overline{u^2}$; the resulting anisotropy causes redistribution from $\overline{u^2}$ to $\overline{w^2}$. 'Superposition' of these two effects is evident in the results presented above. The anisotropy increases monotonically as the free surface is approached. The observed redistribution from $\overline{u^2}$ to $\overline{w^2}$ increases as the anisotropy increases until $z/L \approx 0.1$. Then it decreases, changing sign very near the surface. This near-surface reduction in $\overline{u^2}$ to $\overline{w^2}$ redistribution, in a region of increasing anisotropy, is the effect of the free-surface boundary.

This scenario is evident in the results of Perot & Moin (1993), which show that just after boundary insertion, but before the $\overline{u^2}$ increases significantly, there is substantial $\overline{w^2}$ to $\overline{u^2}$ redistribution at the surface. As time proceeds, and the anisotropy near the surface increases (i.e. as $\overline{u^2}$ increases), the level of $\overline{w^2}$ to $\overline{u^2}$ redistribution decreases.

Hence, we can conclude that the observed behaviour of the Reynolds stresses near the surface results from the reduced dissipation of $\overline{u^2}$, the large decay rate in $\overline{w^2}$ caused by dissipation, and the net transfer of energy between $\overline{w^2}$ and $\overline{u^2}$ through pressure–strain redistribution. The effect of the surface is to cause transfer of energy from $\overline{w^2}$ to $\overline{u^2}$, but this is balanced by transfer from $\overline{u^2}$ to $\overline{w^2}$ caused by the resulting anisotropy. This is consistent with Perot & Moin's (1995) conjecture that the level of pressure–strain redistribution is determined by the balance of 'splat' events and 'anti-splat' events; however, here we propose that the balance is controlled by the local anisotropy for free-surface flows. The role of viscous effects is not clear. (This assumes that their conceptual model is correct.)

This behaviour affects the temporal evolution of the flow. For $\overline{u^2}$, an 'equilibrium' develops where diffusion and turbulent transport rates adjust to the levels of dissipation and redistribution and $\overline{u^2}$ decays on a similar timescale at all locations. The rapid decay of $\overline{w^2}$ near the surface is 'fed' primarily by diffusion of $\overline{w^2}$ to the near-surface region, and by transfer of energy from $\overline{u^2}$ to $\overline{w^2}$. Diffusion of $\overline{w^2}$ to the surface causes the observed anisotropy of the stresses in the centre portion of the computational domain. A further implication of the different decay timescales, is that turbulence near

a free surface cannot decay in a completely self-similar fashion. This may explain the slightly larger decay exponent for the volume-averaged turbulence kinetic energy ($\alpha = 1.088$ *vs.* $\alpha = 1$) discussed above in §2.3.

3.2.4. *Dissipation anisotropy*

Many recent attempts at modelling turbulence near a solid boundary (see e.g. Hanjalic & Launder 1976) and near free surfaces (Swean *et al.* 1991; Miner, Stewart & Swean 1993) have recognized that the dissipation rates for the individual stresses differ. The dissipation rate (term IV of equation (8)) is defined as

$$\epsilon_{ij} = 2\nu \overline{\frac{\partial u_i}{\partial x_k} \frac{\partial u_j}{\partial x_k}}. \tag{23}$$

Conventional approaches to modelling assume that the dissipation is 'isotropic'

$$\begin{aligned} \epsilon_{ij} &= \tfrac{2}{3}\delta_{ij}\epsilon \\ &= \tfrac{2}{3}\delta_{ij}\left(\nu \overline{\frac{\partial u_i}{\partial x_k} \frac{\partial u_i}{\partial x_k}}\right), \end{aligned} \tag{24}$$

where $\epsilon = \frac{1}{2}\epsilon_{ii}$. The anisotropy of the dissipation rate for the Reynolds stresses can be quantified using an anisotropy tensor, similar to that used above in §3.1.1 for the Reynolds stresses (figure 3). This dissipation anisotropy tensor is defined as

$$e_{ij} = \frac{\epsilon_{ij} - \frac{2}{3}\delta_{ij}\epsilon}{\epsilon}, \tag{25}$$

and, as such, is a measure of the deviation of the dissipation rates for the individual stresses from the assumption of isotropic dissipation.

Figure 3 shows the anisotropy of dissipation for $\overline{u^2}$, along with the anisotropy of the Reynolds stress. (Note that, as with the Reynolds stress anisotropy, the surface-normal component is twice the negative of the surface-parallel component.) For $z/L \geqslant 0.75$, the anisotropy in dissipation is negligible. The anisotropy increases gradually as the free surface is approached. For $z/L \leqslant 0.2$, there is a rapid increase to a peak at $z/L = 0.04$, followed by a monotonic decrease to the surface. The behaviour of the anisotropy of dissipation is very different from that of the stresses themselves, both qualitatively and quantitatively. The maximum magnitude of the anisotropy of dissipation is roughly half that for the stresses, and the maximum anisotropy for dissipation occurs at $z/L = 0.04$, while for the stresses, the maximum occurs at the surface.

3.2.5. *Turbulence kinetic energy balance*

The terms in the transport equation for the turbulence kinetic energy are shown in figure 12(*a*). Again, dissipation (term IV) is the dominant term and is roughly equal to $\tilde{\epsilon}$ for $z/L \geqslant 0.2$. The dissipation decreases slowly as the surface is approached to $0.9\,\tilde{\epsilon}$ at $z/L = 0.04$ and then drops sharply to $0.6\,\tilde{\epsilon}$ at the surface. Diffusion (term V) causes a loss of k in the immediate near-surface region, primarily owing to the diffusion of $\overline{u^2}$ away from the surface. For $0.04 \leqslant z/L \leqslant 0.2$ there is a local gain in k owing to diffusion, again reflecting the behaviour of $\overline{u^2}$, while for $z/L \geqslant 0.2$ diffusion is negligible. Near the surface, turbulent transport (term II) causes a loss in k with a peak of $0.4\,\tilde{\epsilon}$ at $z/L = 0.04$. Further from the surface, turbulent transport is small in magnitude and reflects the small variations in the turbulence kinetic energy profile. The

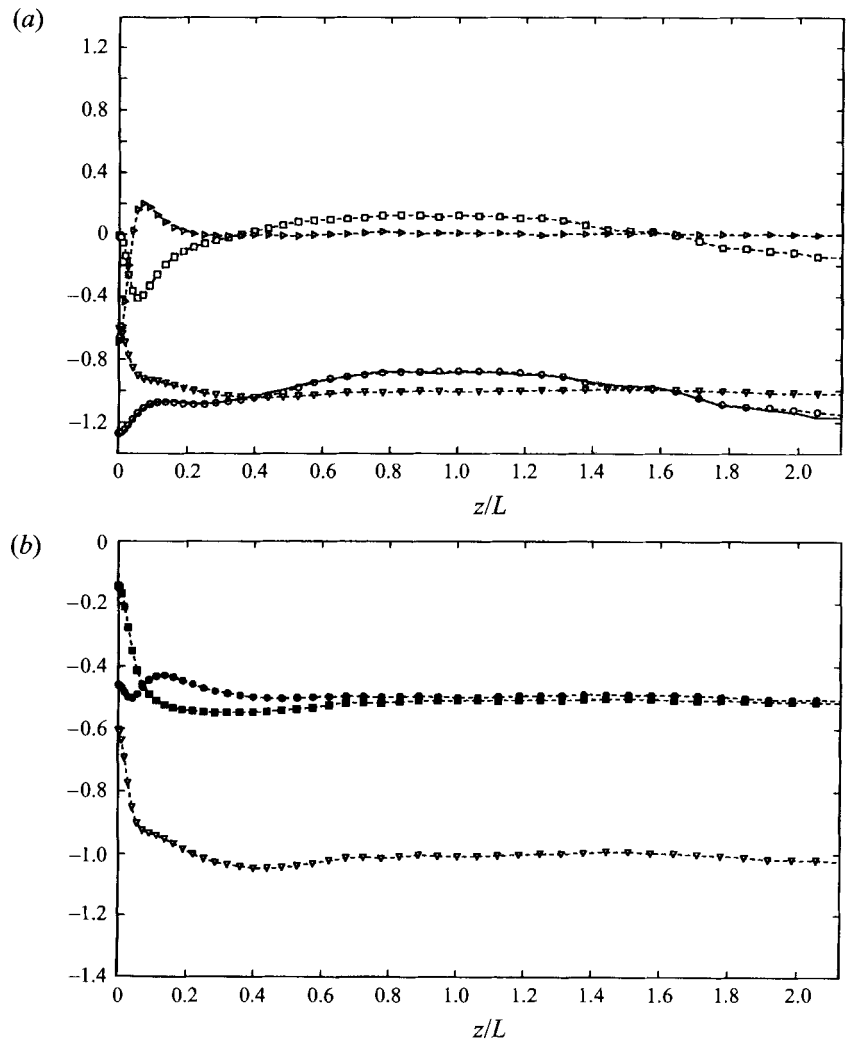

FIGURE 12. (*a*) Terms in (22), the transport equation for the turbulence kinetic energy k, normalized with $\tilde{\epsilon}$; ○, time rate-of-change (term I); □, turbulent transport (term II); ▽, dissipation (term IV); ▷, diffusion (term V); ——, sum of terms II–V. (*b*) Decomposition of the dissipation; ▽, dissipation (term IV); ●, $\nu\overline{S_{ij}S_{ji}}$. ■, $\frac{1}{2}\nu\overline{\omega_i\omega_i}$.

time-rate-of-change in k (term I) reflects the dissipation rate and the turbulent transport for regions far from the surface ($z/L \geqslant 0.2$). Very near the surface diffusion causes an increase in the magnitude of the time derivative. In the intermediate region, gains in k owing to diffusion are offset by losses resulting from turbulent transport. If k were constant, the large losses at the surface owing to diffusion would vanish; hence, the peak in k at the surface results from the reduced level of dissipation.

Figure 12 (*b*) shows the dissipation rate term decomposed into potential strain and rotational contributions:

$$\epsilon = \nu(\overline{S_{ij}S_{ji}} + \tfrac{1}{2}\overline{\omega_i\omega_i}). \tag{26}$$

From the figure it is clear that the reduction in dissipation at the surface is mainly due to the decrease in enstrophy at the surface.

3.3. *Fluctuating enstrophy balance*

The shear-free boundary condition specified in this simulation allows vorticity normal to the free surface, but the tangential vorticity must vanish at the surface. The physical manifestations of this boundary condition are the attached vorticity distributions observed in free-surface experiments (Madnia & Bernal 1994; Walker *et al.* 1995). The interaction of the vorticity field with the boundary can be studied using the balance equations for the total enstrophy $\frac{1}{2}\overline{\omega_i\omega_i}$, and those for the tangential and surface-normal components, $\overline{\omega_x^2}$ and $\overline{\omega_z^2}$.

The balance equations are derived in the same manner as the balance equations for the components of the Reynolds stress tensor. The details of the derivation of the balance equation for the fluctuating enstrophy are contained in Balint, Vukoslavcevic & Wallace (1988). The enstrophy balance equation for a flow with zero mean velocity is

$$\underbrace{\frac{\partial}{\partial t}\overline{\frac{\omega_i\omega_i}{2}}}_{\text{I}} = \underbrace{-\frac{\partial}{\partial x_j}\overline{\frac{u_j\omega_i\omega_i}{2}}}_{\text{II}} + \underbrace{\overline{\omega_i\omega_j\frac{\partial u_i}{\partial x_j}}}_{\text{III}} \underbrace{-\nu\overline{\frac{\partial\omega_i}{\partial x_j}\frac{\partial\omega_i}{\partial x_j}}}_{\text{IV}} + \underbrace{\nu\frac{\partial^2}{\partial x_j^2}\overline{\frac{\omega_i\omega_i}{2}}}_{\text{V}}, \tag{27}$$

with an implied summation on i for the total fluctuating enstrophy $\frac{1}{2}\overline{\omega_i\omega_i}$, and no summation for the components of enstrophy. According to Tennekes & Lumley (1972) and Balint *et al.* (1988), the terms of the enstrophy balance equation have the following interpretation: the local rate of change of the enstrophy (term I), transport of enstrophy by fluctuating velocity (term II), production by turbulent fluctuations (term III), viscous dissipation (term IV), and viscous diffusion (term V).

The production terms (III) are different in character from any terms which were examined in the Reynolds stress transport equations above. The velocity gradient tensor in term III of (27) can be decomposed into symmetric and antisymmetric parts to yield

$$\overline{\omega_i\omega_j\frac{\partial u_i}{\partial x_j}} = \overline{\omega_i\omega_j S_{ij}} + \overline{\omega_i\omega_j W_{ij}}, \tag{28}$$

where S_{ij} is the strain-rate tensor, defined in (16) above, and

$$W_{ij} = \frac{1}{2}\left(\frac{\partial u_i}{\partial x_j} - \frac{\partial u_j}{\partial x_i}\right) \tag{29}$$

is the rotation-rate tensor. The quantity $\omega_j W_{ij}$ is identically zero (it reduces to the cross-product of the vorticity with itself) and so (28) reduces to

$$\overline{\omega_i\omega_j\frac{\partial u_i}{\partial x_j}} = \overline{\omega_i\omega_j S_{ij}}. \tag{30}$$

Hence, the production terms represent interactions between the vorticity field and the fluctuating irrotational strain field. For $i = j$ in (30) the terms are usually referred to as 'vortex-stretching' terms since they involve the normal strain rate. For $i \neq j$, they are often called 'vortex-tilting' terms. Since the term involving the rotation rate tensor W_{ij} vanishes, there is no inter-component transfer of vorticity owing to the rotation of the vorticity vector owing to local fluid rotation.

The 'stretching' and 'tilting' terms are actually different manifestations of the same process. If we consider vorticity components resolved into a coordinate system aligned

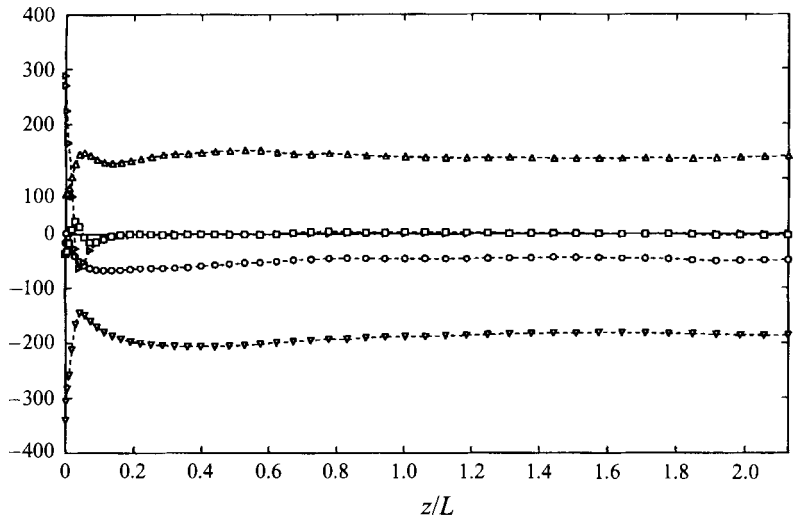

FIGURE 13. Terms in (31), the transport equation for the fluctuating enstrophy $\frac{1}{2}\overline{\omega_i\omega_i}$, normalized with $\tilde{\epsilon}^3/\tilde{k}^3$; ○, time rate-of-change (term I); □, turbulent transport (term II); △, turbulent production (term III); ▽, dissipation (term IV); ▷, diffusion (term V).

with the principal axes of S_{ij}, there will be production (or destruction) of vorticity components owing to stretching (or compression). In this case, the terms in (30) for $i \neq j$ will vanish, and the interpretation of the remaining terms is clear. For an arbitrary coordinate system, the $i \neq j$ terms will not vanish, but the interpretation is the same, nonetheless. If, owing to a boundary condition, the principal axes of S_{ij} tend to align with the coordinate system chosen (i.e. if the shear strains vanish), then the $i \neq j$ terms will vanish.

For the flow in question, total fluctuating enstrophy balance (27) reduces to

$$\underbrace{\frac{\partial}{\partial t}\frac{\overline{\omega_i\omega_i}}{2}}_{\text{I}} = \underbrace{-\frac{\partial}{\partial z}\frac{\overline{w\omega_i\omega_i}}{2}}_{\text{II}} + \underbrace{\overline{\omega_i\omega_j S_{ij}}}_{\text{III}} \underbrace{-\nu\overline{\frac{\partial\omega_i}{\partial x_j}\frac{\partial\omega_i}{\partial x_j}}}_{\text{IV}} + \underbrace{\nu\frac{\partial^2}{\partial z^2}\frac{\overline{\omega_i\omega_i}}{2}}_{\text{V}}. \tag{31}$$

The balance equation for the surface-parallel vorticity component $\frac{1}{2}\overline{\omega_x^2}$ is given by

$$\underbrace{\frac{\partial}{\partial t}\overline{\omega_x^2}}_{\text{I}} = \underbrace{-\frac{\partial}{\partial z}\overline{w\omega_x^2}}_{\text{II}} + \underbrace{2\overline{\omega_x\omega_x S_{xx}} + 2\overline{\omega_x\omega_y S_{xy}} + 2\overline{\omega_x\omega_z S_{xz}}}_{\text{III}} \underbrace{-2\nu\overline{\frac{\partial\omega_x}{\partial x_j}\frac{\partial\omega_x}{\partial x_j}}}_{\text{IV}} + \underbrace{\nu\frac{\partial^2}{\partial z^2}\overline{\omega_x^2}}_{\text{V}}, \tag{32}$$

and that for the surface-normal component $\frac{1}{2}\overline{\omega_z^2}$ is given by

$$\underbrace{\frac{\partial}{\partial t}\overline{\omega_z^2}}_{\text{I}} = \underbrace{-\frac{\partial}{\partial z}\overline{w\omega_z^2}}_{\text{II}} + \underbrace{2(\overline{\omega_z\omega_x S_{zx}} + \overline{\omega_z\omega_y S_{zy}}) + 2\overline{\omega_z\omega_z S_{zz}}}_{\text{III}} \underbrace{-2\nu\overline{\frac{\partial\omega_z}{\partial x_j}\frac{\partial\omega_z}{\partial x_j}}}_{\text{IV}} + \underbrace{\nu\frac{\partial^2}{\partial z^2}\overline{\omega_z^2}}_{\text{V}}. \tag{33}$$

In (32) and (33), a factor of two has been introduced. In this final equation, the

production terms involving the shear strains will be considered collectively, since they will be equal owing to the requirement of rotational symmetry for the statistics in planes parallel to the free surface.

3.3.1. *Terms of the fluctuating enstrophy balance*

The terms of the enstrophy balance (31) are shown in figure 13, where the terms have been normalized with $(\tilde{\epsilon}/\tilde{k})^3$. In the centre portion of the domain, turbulent production makes a substantial positive contribution to $\frac{1}{2}\overline{\omega_i\omega_i}$. The rate of dissipation exceeds production and, as a result, the enstrophy level is decaying. The viscous diffusion and turbulent transport are negligible in the core of the flow. As the shear-free boundary is approached, these terms become larger and there are significant changes in dissipation and diffusion. The region in which the deviations occur is thin, much thinner than the region in which the tangential vorticity fluctuations go to zero. The total enstrophy production level decreases by nearly 50% as the surface is approached. There is a 75% increase in the dissipation rate at the surface. This increase in dissipation is partially offset by a near-surface gain in $\frac{1}{2}\overline{\omega_i\omega_i}$ owing to diffusion.

3.3.2. *Terms of the tangential enstrophy component balance*

The behaviour of the terms of (32) the balance of the tangential vorticity fluctuations $\overline{\omega_x^2}$ is shown in figure 14(*a*). For $z/L \geqslant 0.2$ the transport (term II) and diffusion (term V) are zero and the variation in the remaining terms is small. The balance of $\overline{\omega_x^2}$ at the shear-free boundary reflects the zero-tangential-vorticity condition discussed above. Near the free surface there is a loss of $\overline{\omega_x^2}$ owing to diffusion, with a maximum at approximately $z/L \approx 0.05$. At the surface there is a significant gain in $\overline{\omega_x^2}$ owing to diffusion. Hence, the vanishing of tangential vorticity at the surface causes diffusive transport of $\overline{\omega_i^2}$ from points near the boundary to the boundary. The dissipation (term IV) and diffusion terms must balance at the boundary; hence, the transport of $\overline{\omega_x^2}$ to the boundary by diffusion is balanced locally by the dissipation. While this balance applies strictly only at the boundary, it appears that the variations in diffusion are balanced by the variations in dissipation near the boundary as well. The turbulent transport of $\overline{\omega_i^2}$ exhibits a maximum near the surface which is the result of the large vertical gradient in the vorticity fluctuations near the boundary. Although the surface-normal velocity fluctuations are small near the boundary, the large (negative) gradient in $\overline{\omega_x^2}$ will result in significant transport. The transport, however, must also be zero at the boundary. The production of $\overline{\omega_x^2}$ (term III) is approximately uniform from $z/L \approx 0.6$ to the centre of the domain. Between $z/L \approx 0.1$ and $z/L \approx 0.6$ the turbulent production is elevated by about 10%. Since the tangential vorticity on the boundary is zero, production must vanish there. Near the boundary the production approaches zero rapidly.

It appears, then, that the level of the tangential enstrophy component near the surface is maintained by near-surface production. Turbulent transport and viscous diffusion move tangential enstrophy to the surface and here it is dissipated.

The production term, decomposed into its components, is shown in figure 14(*b*). The production by stretching (S_{xx}) has a maximum near the surface, then decreases by 30% and is roughly constant for $z/L \geqslant 0.1$. The thin production region is smaller in extent, by approximately a factor of two, than the value of the lateral microscale associated with the tangential vorticity λ_{gw}. This is consistent with the observed reduction in longitudinal microscale λ_f at the shear-free boundary (shown in figure 5), and the increase in normal-strain-rate fluctuations near the surface (shown in figure 8). The production term related to the S_{xy} shear strains is the next major contributor to $\overline{\omega_x^2}$. As

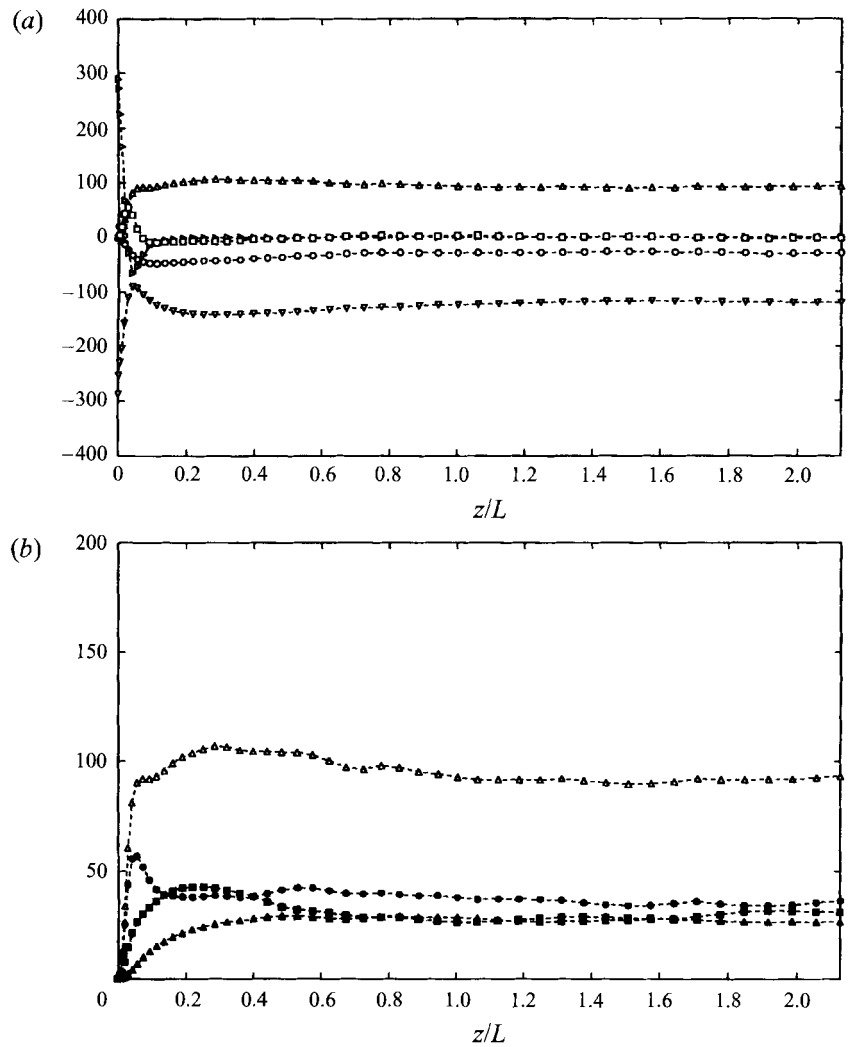

FIGURE 14. Terms in (32), the transport equation for $\overline{\omega_x^2}$, and decomposition of the turbulent production term, normalized with $\tilde{\epsilon}^3/\tilde{k}^3$; (*a*) terms in the transport equation for $\overline{\omega_x^2}$; ○, time rate-of-change (term I); □, turbulent transport (term II); △, turbulent production (term III); ▽, dissipation (term IV); ▷, diffusion (term V); (*b*) decomposition of the turbulent production term; △, turbulent production; ●, $\overline{\omega_x \omega_x S_{xx}}$; ■, $\overline{\omega_x \omega_y S_{xy}}$; ▲, $\overline{\omega_x \omega_z S_{xz}}$.

the free surface is approached, the production rises over the region $z/L \approx 0.1$–0.5, and has its maximum at the location where $\overline{\omega_x^2}$ peaks, before going to zero at the boundary, where $\omega_x = \omega_y = 0$. Significant shearing strains in the (x, y)-plane result when the in-plane principal strain rates are substantially different, such as in regions of stagnation, and tend to align the vorticity vector with the direction of the maximum (most positive) principal strain. The remaining production term is the production of $\overline{\omega_x^2}$ owing to the S_{xz} shear strain. This term goes to zero as the surface is approached since S_{xz} and ω_x are required to vanish at the surface.

The increased production due to stretching (S_{xx}) and shear in the (x, y)-plane (S_{xy}) can be explained in terms of simple physical models. The increased production of $\overline{\omega_x^2}$ owing to stretching near the surface is due to the impact of fluid moving up from below on the free surface. This event is termed a 'splat' event by Leighton *et al.* (1991), based

on a description in Bradshaw & Koh (1981). When upward-moving fluid reaches the surface, the streamlines will diverge from a stagnation point and near-surface tangential vorticity will be stretched by the diverging flow. This intensification process is limited by viscous dissipation and diffusion. The production of $\overline{\omega_x^2}$ owing to S_{xy} indicates that large shearing strains, typical of regions of stagnation, can occur in planes parallel to the free surface. In the discussion of figure 7 in §3.1.3, above, evidence was presented which indicated that there was increased correlation between the surface-parallel vorticity and velocity owing to the presence of the free-surface boundary. It was proposed that this resulted from mutual induction between surface-parallel vorticity and its 'image' above the free surface. A vortex filament moving due to this type of interaction will create regions of stagnation ahead of it, and behind it. This type of structure, therefore, could lead to production due to S_{xy}. The lack of significant production due to S_{xz} indicates that near the surface, the local vorticity vector tends to be oriented either normal to the free surface, or parallel to the free surface.

3.3.3. *Terms of the surface-normal enstrophy component balance*

The terms of (33), the $\overline{\omega_z^2}$ balance, are shown in figure 15(*a*). All terms are constant for $z/L \geqslant 0.6$, and are similar in magnitude to the tangential case, as would be expected for homogeneous, isotropic turbulence. Dissipation (term IV) varies only slightly as the surface is approached, and diffusion (term V) is near zero everywhere, since $\overline{\omega_z^2}$ is nearly constant. This is due to the requirement that the surface-normal gradient of ω_z, rather than ω_z itself vanish at the surface. The effect of the surface as observed in the production and transport terms extends to about $z/L = 0.6$, more than twice the lateral microscale. As the surface is approached, the turbulent production (term III) decreases slightly to a local minimum at $z/L \approx 0.2$, and then increases to a maximum at the surface. The maximum is 50% larger than the production level far from the surface. The turbulent transport of $\overline{\omega_z^2}$ (term II) is negative for $0 \leqslant z/L \leqslant 0.1$ and is then positive and decaying until $z/L \approx 0.4$. Far from the surface, the turbulent transport is zero, as expected since there is no gradient in $\overline{\omega_z^2}$. This implies that $\overline{\omega_z^2}$ is being transported from near the surface to a thin region below the surface.

The production of $\overline{\omega_z^2}$ by shear is shown in figure 15(*b*) along with the term representing production of $\overline{\omega_z^2}$ by normal stretching. For $z/L \geqslant 0.7$, 40% of the turbulent production of the correlation comes from stretching (S_{zz}). This is the same as observed in the tangential components. As the free surface is approached, the production by shear decreases to zero. Again, this is a result of the shear-free nature of the boundary, where $S_{xz} = S_{yz} = 0$ and $\omega_x = 0$. The stretching term initially decreases, achieving a minimum at $z/L \approx 0.2$. As the shear-free boundary is approached, production due to S_{zz} increases; this indicates that the surface-normal vorticity is correlated with positive vertical velocities (away from the surface). It was noted above that the variations in production were roughly offset by the turbulent transport of $\overline{\omega_z^2}$. This is because the same downward flow which contributes to the production of $\overline{\omega_z^2}$ through vortex stretching also transports $\overline{\omega_z^2}$ away from the surface. As a result the near-surface variations of these two terms can be expected to be substantially in balance. This indicates that the level of the mean-square surface-normal vorticity is largely unaffected by the free-surface boundary.

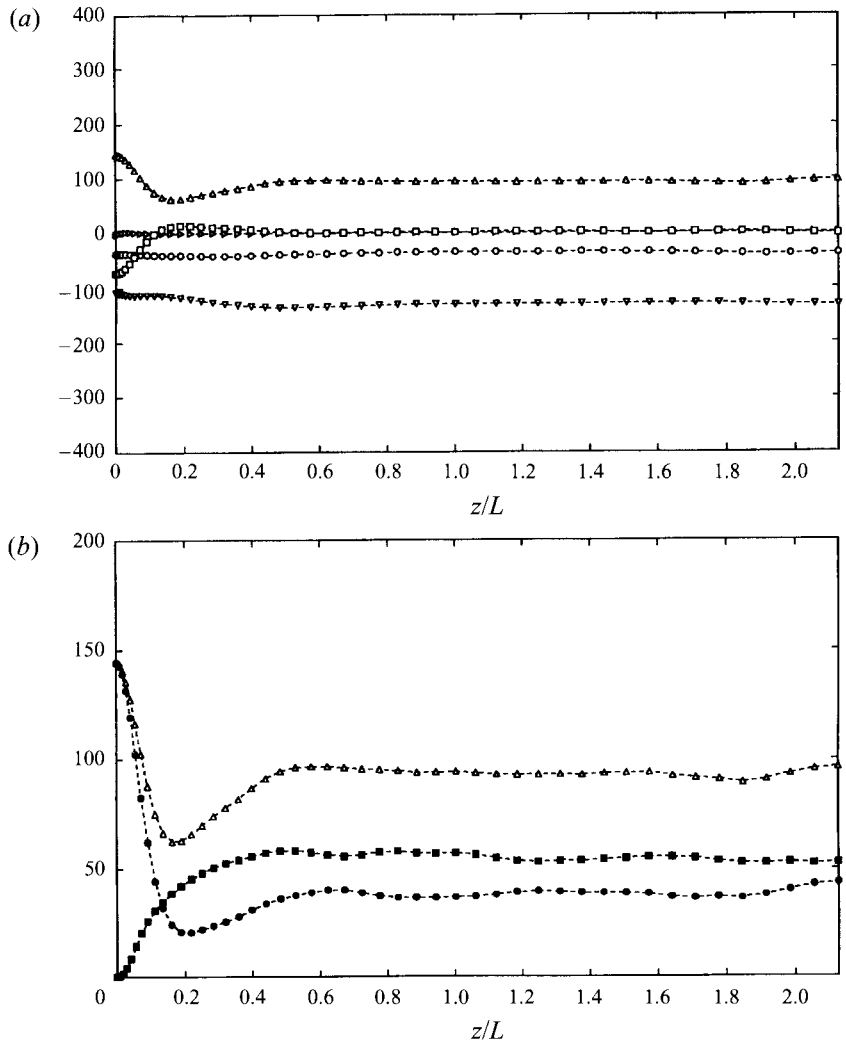

FIGURE 15. Terms in (33), the transport equation for $\overline{\omega_z^2}$, and decomposition of the turbulent production term, normalized with $\tilde{\epsilon}^3/\tilde{k}^3$; (*a*) terms in the transport equation for $\overline{\omega_z^2}$; ○, time rate-of-change (term I); □, turbulent transport (term II); △, turbulent production (term III); ▽, dissipation (term IV); ▷, diffusion (term V); (*b*) decomposition of the turbulent production term; △, turbulent production; ●, $\overline{\omega_z \omega_z S_{zz}}$; ■, $\overline{\omega_z \omega_x S_{zx}} + \overline{\omega_z \omega_y S_{zy}}$.

4. Summary and conclusions

In this study the evolution of initially homogeneous and isotropic turbulence in the presence of a free surface was investigated. The purpose was to examine the interaction of turbulence with a free surface in the absence of mean velocity gradients, so that the interaction of the turbulence with the free surface could be separated from the interaction of the mean flow and the free surface.

The Navier–Stokes equations were solved via direct pseudo-spectral simulation with a resolution of 96^3. The computational domain was a cube $4.25L$ on a side, where $L = \tilde{k}/\tilde{\epsilon}^{3/2}$ is the turbulent lengthscale where $\tilde{k}$ and $\tilde{\epsilon}$ are the volume-averaged turbulence kinetic energy and dissipation rate. Periodic boundary conditions were used in two dimensions, and the top and bottom sides of the domain were flat and shear-

free. A random, divergence-free velocity field with a prescribed spectrum was used as the initial conditions. After evolving for five time units, where time is normalized by the initial r.m.s. velocity and integral lengthscale, this 'base' velocity field was used to generate statistically independent velocity fields for an ensemble of sixteen separate simulations. This ensemble was allowed to evolve for an additional five time units. Statistics were then calculated by ensemble averaging and averaging over a short time (approximately half the 'eddy-turnover' time). For the time period examined, the Reynolds number based on $\tilde{k}$ and $\tilde{\epsilon}$ was 147.

The time evolution of the base flow was examined and shown to be consistent with the theoretical results of Speziale & Bernard (1992) for the decay of isotropic turbulence. The palinstrophy coefficient was sufficiently high to ensure self-preserving behaviour if there were no boundaries present. The decay rate for the volume-averaged turbulence kinetic energy was $t^{-1.088}$, slightly more rapid than the t^{-1} behaviour predicted by the theory. The large decay rate for $\overline{w^2}$ near the surface may explain this small deviation from the theory.

Near the surface, the Reynolds stresses are anisotropic, owing to the requirement that w vanish at the surface. The anisotropy extends a distance from the surface roughly equal to L. The tangential vorticity fluctuations also vanish at the surface, owing to the no-shear condition. The reduction in tangential vorticity fluctuations at the surface results in a corresponding decrease in the enstrophy. The region in which the surface affects the vorticity distribution is roughly $0.1L$, much thinner than the region of anisotropy for the velocity fluctuations. Examination of the velocity–vorticity correlations showed that there is significant interaction of tangential vorticity with the boundary.

For the surface-normal velocity fluctuations, the pressure transport and the turbulent transport due to velocity fluctuations roughly balance and result in little net turbulent transport. The anisotropy level near the surface appears to be maintained by a reduction in dissipation for the tangential velocity fluctuations near the surface, a reduction in pressure–strain transfer from the larger tangential velocity fluctuations to the smaller surface-normal velocity fluctuations caused by the surface, and the rapid temporal decay of the surface-normal velocity fluctuations near the surface owing to the fact that the surface-normal velocity vanishes, while its dissipation rate remains finite.

The turbulence kinetic energy rises in the near-surface region owing to a decrease in dissipation at the surface. This decrease in dissipation results from a local reduction in enstrophy. Near the free surface, the mean pressure rises, owing also to the reduction in enstrophy. The low-level enstrophy near the surface results from the requirement that its tangential component vanish at the surface. The level of tangential enstrophy in the near-surface region is maintained by the losses caused by diffusion and dissipation near the surface, and by the lack of production at the surface.

The results of this study also indicate that, while the tangential vorticity must vanish at the free surface, the flow is fully three-dimensional up to the surface and that the production of surface-normal vorticity by vortex stretching (which is inconsistent with the idea of two-dimensional turbulence) attains a maximum at the free surface. The contribution to the total enstrophy by the surface-normal vorticity fluctuations remains relatively constant over depth, which is in contrast to the results of Gharib *et al.* (1994). In the overall surface-normal enstrophy component balance the production due to vortex stretching is roughly balanced by turbulent transport of enstrophy away from the surface and so the level of surface-normal vorticity fluctuations remains relatively constant in space and decays uniformly on time.

There is elevated production of tangential vorticity near the surface by vortex-stretching, and by the fluctuating shear strains. The former effect is due to tangential vorticity being affected by the normal strains associated with 'splat' events. The latter effect is associated with structures comprised of tangential vorticity moving parallel to the surface owing to mutual induction with their 'images'. The stagnation regions ahead and behind these structures give rise to regions of high shear strain (in planes parallel to the free surface), and may result in large production of tangential vorticity by 'tilting'.

This work was supported by the National Science Foundation's Pittsburgh Supercomputing Center, Grant No. CBT910031P, and in part by the Fluid Dynamics Program of the Office of Naval Research under Grant Number N00014-92-J-1750, monitored by Dr E. P. Rood, as well as the Fluid Dynamics Task Area at the Naval Research Laboratory.

REFERENCES

ANTHONY, D. G. & WILLMARTH, W. W. 1992 Turbulence measurements in a round jet near a free surface. *J. Fluid Mech.* **243**, 699.

BALINT, J.-L., VUKOSLAVCEVIC, P. & WALLACE, J. M. 1988 The transport of enstrophy in a turbulent boundary layer. *Proc. Zaric Memorial Intl Seminar on Wall Turbulence* (ed. S. J. Kline). Dubrovnik.

BETCHOV, R. 1956 An inequality concerning the production of vorticity in isotropic turbulence. *J. Fluid Mech.* **1**, 497.

BRADSHAW, P. & KOH, Y. M. 1981 A note on Poisson's equation for pressure in a turbulent flow. *Phys. Fluids* **24**, 777.

BRUMLEY, B. H. & JIRKA, G. H. 1987 Near-surface turbulence in a grid-stirred tank. *J. Fluid Mech.* **182**, 235.

GHARIB, M., DABIRI, D. & ZHANG, X. 1994 Interaction of small-scale turbulence with a free surface. In *Free-Surface Turbulence* (ed. E. P. Rood & J. Katz). ASME FED-181, p. 97.

GREENBERG, M. D. 1971 *Application of Green's Functions in Science and Engineering.* Prentice-Hall.

HANDLER, R. A., SWEAN, T. F., LEIGHTON, R. I. & SWEARINGEN, J. D. 1993 Length scales and the energy balance for turbulence near a free surface. *AIAA J.* **31**, 1998.

HANJALIC, K. & LAUNDER, B. E. 1976 Contribution towards a Reynolds-stress closure for low-Reynolds-number turbulence. *J. Fluid Mech.* **74**, 593.

HINZE, J. O. 1975 *Turbulence.* McGraw-Hill, New York.

HUNT, J. C. R. 1984 Turbulence structure in thermal convection and shear-free boundary layers. *J. Fluid Mech.* **138**, 161.

HUNT, J. C. R. & GRAHAM, J. M. R. 1978 Free-stream turbulence near plane boundaries. *J. Fluid Mech.* **84**, 209.

KAMBE, T. 1984 Some dissipation mechanisms in vortex systems. *Turbulence and Chaotic Phenomena in Fluids* (ed. T. Tatsumi), p. 239. Elsevier.

KERR, R. M. 1985 Higher-order derivative correlations and the alignment of small-scale structures in isotropic numerical turbulence. *J. Fluid Mech.* **153**, 31.

KIM, J., MOIN, P. & MOSER, R. D. 1987 Turbulence statistics in fully developed channel flow at low Reynolds number. *J. Fluid Mech.* **177**, 133.

LAM, K. & BANERJEE, S. 1988 Investigation of turbulent flow bounded by a wall and a free surface. In *Fundamentals of Gas-Liquid Flows* (ed. E. Michaelides & M. P. Sharma). ASME FED-72, p. 29.

LAUNDER, B. E. 1990 Phenomenological modeling: Present...and future? *Whither Turbulence? Turbulence at the Crossroads* (ed. J. L. Lumley). Lecture Notes in Physics, vol. 357, p. 439. Springer.

LEIGHTON, R. I., HANDLER, R. A., SWEAN, T. F. & SWEARINGEN, J. 1991 Interaction of vorticity with a free surface in turbulent open channel flow. *AIAA Paper* 91-0236.

LEIPMANN, D. & GHARIB, M. 1994 The vorticity and entrainment dynamics of near-surface jets. In *Free-Surface Turbulence* (ed. E. P. Rood & J. Katz). ASME FED-181, p. 53.

MADNIA, K. & BERNAL, L. P. 1994 Interaction of a turbulent round jet with the free surface. *J. Fluid Mech.* **261**, 305.

MANGIAVACCHI, N., GUNDLAPALLI, R. & AKHAVAN, R. 1994 Dynamics of a turbulent jet interacting with a free surface. In *Free-Surface Turbulence* (ed. E. P. Rood & J. Katz). ASME FED-181, p. 69.

MINER, E. W., STEWART, M. B. & SWEAN, T. F. 1993 Modeling and computation of turbulent free-surface jets. *AIAA Paper* 93-0201.

NEWMAN, G. R. & LUMLEY, J. L. 1977 Return to isotropy of homogeneous turbulence. *J. Fluid Mech.* **82**, 161.

ORSZAG, S. A. 1969 Numerical methods for the simulation of turbulence. *Phys. Fluids Suppl. II*, II-250.

ORSZAG, S. A. & PATERA, A. T. 1983 Secondary instability of wall-bounded shear flows. *J. Fluid Mech.* **128**, 347.

PEROT, J. B. & MOIN, P. 1993 Shear-free turbulent boundary layers: Physics and modeling. *Rep. TF-60*, Thermosciences Division, Department of Mechanical Engineering, Stanford University.

PEROT, J. B. & MOIN, P. 1995 Shear-free turbulent boundary layers. Part 1. Physical insights into near-wall turbulence. *J. Fluid Mech.* **295**, 199.

SPEZIALE, C. G. & BERNARD, P. S. 1992 The energy decay in self-preserving isotropic turbulence revisited. *J. Fluid Mech.* **241**, 645.

SWEAN, T. F., LEIGHTON, R. I., HANDLER, R. A. & SWEARINGEN, J. D. 1991 Turbulence modeling near the free surface in open channel flow. *AIAA Paper* 91-0613.

SWEAN, T. F., RAMBERG, S. E., PLESNIA, M. W. & STEWART, M. B. 1989 Turbulent surface jet in a channel of limited depth. *J. Hydraul. Engng ASCE* **115**, 1587.

TENNEKES, H. & LUMLEY, J. L. 1972 *A First Course in Turbulence*. MIT Press.

THOMAS, N. H. & HANCOCK, P. E. 1977 Grid generated turbulence near a moving wall. *J. Fluid Mech.* **82**, 481.

UZKAN, T. & REYNOLDS, W. C. 1967 A shear-free turbulent boundary layer. *J. Fluid Mech.* **82**, 481.

WALKER, D. T., CHEN, C.-Y. & WILLMARTH, W. W. 1995 Turbulent structure in free-surface jet flows. *J. Fluid Mech.* **291**, 223.